Journal of Computational Physics 231 (2012) 4613–4642

Contents lists available at SciVerse ScienceDirect

Journal of Computational Physics

journal homepage: www.elsevier.com/locate/jcp

An immersed boundary energy-based method for incompressible viscoelasticity

Dharshi Devendran *, Charles S. Peskin

Courant Institute of Mathematical Sciences, 251 Mercer Street, New York, NY 10012, USA

ARTICLE INFO

Article history:
Received 29 April 2011
Received in revised form 29 November 2011
Accepted 28 February 2012
Available online 5 April 2012

Keywords:
Immersed boundary method
Incompressible viscoelasticity
Energy-based method
Fluid–structure interaction

ABSTRACT

Incompressible viscoelastic materials are prevalent in biological applications. In this paper we present a method for incompressible viscoelasticity in which the elasticity of the material is described in Lagrangian form (i.e. in material coordinates), and Eulerian (spatial) coordinates are used for the equations of motion and to enforce the incompressibility condition. The elastic forces are computed directly from an energy functional without the use of stress tensors, and the immersed boundary method is used to communicate between Lagrangian and Eulerian variables. The method is first applied to a warm-up problem, in which a viscoelastic incompressible material fills a two-dimensional periodic domain. For this problem, we study convergence of the velocity field, the deformation map, and the Eulerian force density. The numerical results indicate that the velocity field and deformation map converge strongly at second order and the Eulerian force density converges weakly at second order. Incompressibility is well maintained, as indicated by area conservation in this 2D problem. Finally, the method is applied to a three-dimensional fluid–structure interaction problem with two different materials: an isotropic neo-Hookean model and an anisotropic fiber-reinforced model.

1. Introduction

Incompressible viscoelastic materials are present in a variety of applications. Biological tissue, for example, is often modeled as an incompressible viscoelastic material. Computing the motion of these materials is difficult because elastic forces are most naturally described in Lagrangian (material) coordinates whereas the incompressibility constraint and the viscous forces are most simply described in Eulerian (spatial) coordinates.

In this paper, we introduce a method for incompressible viscoelasticity that formulates the elastic forces in terms of Lagrangian coordinates and the equations of motion, the incompressibility condition, and the viscous forces in terms of Eulerian coordinates. To convert from one coordinate system to the other one, we use the numerical apparatus of the immersed boundary method [3]. The Lagrangian part of our method resembles finite element methods for elasticity in that we use a triangular (in 2D) or tetrahedral (in 3D) Lagrangian mesh and describe deformations by piecewise linear functions. There are no stress tensors in our formulation, however. Instead, the elastic forces are computed directly from an energy functional. Finally, the equations remain in their strong form, so no system of equations involving the mass matrix needs to be solved.

In Section 2, we derive our model of incompressible viscoelasticity. First, we give a description of the elastic forces in terms of the derivative of an energy functional and explain how this formulation relates to the more conventional stress-based formulation of elasticity. Our definition of the elastic forces is given in material coordinates. Next, we write the equations of motion for the elastic material and incompressibility constraint in spatial coordinates. The equations of

* Corresponding author.
E-mail address: dharshi@cims.nyu.edu (D. Devendran).

0021-9991/$ - see front matter © 2012 Elsevier Inc. All rights reserved.
http://dx.doi.org/10.1016/j.jcp.2012.02.020

motion include a forcing term to account for the elastic forces. At this point, we introduce the immersed boundary method to compute this Eulerian forcing term from the elastic forces defined in Lagrangian coordinates.

In Section 3, we present a discretization of our model. We approximate the deformation map by a piecewise linear function and use this approximation to compute the forces in material coordinates. These computations take place on a tetrahedral mesh in three dimensions and a triangular mesh in two dimensions. The Eulerian equations of motion are discretized using finite differences over a Cartesian staggered grid. The immersed boundary method is the mechanism by which we transfer information from the triangular or tetrahedral mesh to the staggered grid and vice versa.

Finally, we present our numerical results in Section 4. We begin with our two-dimensional results in which a viscoelastic material fills a periodic domain. The elastic material is initially undeformed, but it is given a nonzero initial velocity. The material deforms under this velocity, and generates elastic forces that result in a damped oscillation around the reference configuration. We simulate this problem under two choices of the elastic energy functional: a linear elasticity model and a neo-Hookean model. The linear elasticity model is applied to a case with small displacements and the neo-Hookean model to one with large displacements.

For this problem, we perform an area conservation study in which we compare the area of a material disk with its initial area as it deforms. The results of this study indicate that incompressibility is well maintained by the method. We also study convergence of the velocity field, the deformation map, and the elastic force density on the Eulerian grid, for both choices of the elastic energy functional. Our results indicate that the velocity field and deformation map converge strongly at second order, and that the Eulerian force density converges weakly at second order.

Finally, we apply our method to a large-deformation fluid–structure interaction problem in three dimensions. An incompressible viscoelastic thick shell is immersed in incompressible fluid. The system is given an initial velocity which deforms the elastic shell and consequently generates elastic forces in the shell. These elastic forces give rise to large-amplitude damped motions of the elastic shell about its reference configuration.

We simulate this problem under two material models for the thick elastic shell: a three-dimensional isotropic neo-Hookean model and an anisotropic material model. This example demonstrates the ease with which one material model can be switched for another model within the framework of the present paper. This is an advantage in comparison to the more traditional immersed boundary method [1] in which elastic materials are modeled as networks of (possibly nonlinear) springs. Such networks have to be designed anew for each case, their parameters are not related in an obvious way to the elastic moduli of the continuum description, and it is especially difficult to simulate an isotropic material undergoing large deformations as a network of springs.

Our method is not the first immersed boundary method to use a finite-element-like discretization of the elastic material, in which forces are computed by taking the derivative of an energy function [16]. In the present paper, however, we put the entire burden of enforcing incompressibility on the Eulerian fluid solver, without any need for an auxiliary pressure associated with the elastic material, and we demonstrate the simplicity with which it is possible to replace one hyperelastic material model by another within the framework of our finite-element-like discretization. Also, the method introduced in [16] is applied only to examples in two dimensions. Here, we present an application to a three-dimensional fluid-structure interaction problem. Finally, the present paper contains the first application of the immersed boundary method to a pure incompressible viscoelasticity problem, without any physical fluid. This application provides the setting for a convergence study, which demonstrates empirical second-order accuracy of the immersed boundary method when used in this manner, i.e., in the absence of fluid-structure interfaces. This convergence study, moreover, raises an interesting theoretical issue, the weak convergence of the force density that accompanies the strong convergence of the velocity and displacement fields.

2. Model derivation

In this section we derive our energy-based model for incompressible viscoelasticity. The equation of motion for a viscoelastic solid in spatial coordinates is given by

$$\rho \frac{D\mathbf{v}}{Dt} = \nabla_{\mathbf{x}} \cdot \sigma^e + \nabla_{\mathbf{x}} \cdot \sigma^v \tag{1}$$

where $\mathbf{v}(\mathbf{x},t)$ is the velocity of the material points expressed as a function of fixed position $\mathbf{x}$ and time t, ρ is the density, σ^e is the Cauchy stress tensor that describes the elastic stresses, and σ^v is the Cauchy stress tensor that describes the viscous forces. For now we allow compressibility and specialize to the incompressible case later.

In the following, we use $\mathbf{x}$ to denote spatial coordinates and $\mathbf{s}$ to denote material coordinates. For clarity, we also emphasize the variable of differentiation in the differentiation operators. For example, $\nabla_{\mathbf{x}}$ denotes the gradient with respect to $\mathbf{x}$.

Recall that

$$\frac{D\mathbf{v}}{Dt} = \frac{\partial \mathbf{v}}{\partial t} + \mathbf{v} \cdot \nabla_{\mathbf{x}} \mathbf{v} \tag{2}$$

is the material derivative of $\mathbf{v}$; that is, it is the time derivative of $\mathbf{v}$ following the material points.

Our goal is to replace $\nabla_{\mathbf{x}} \cdot \sigma^e$ with forces that can be calculated directly from an energy functional. For this purpose, let us assume that we have a hyperelastic material. Hyperelastic means the constitutive law for the stress tensors is given in terms of a stored energy potential $W = W(\mathbb{F})$. Here, $\mathbb{F}$ is the deformation gradient whose components are given by $\mathbb{F}_{ij} = \frac{\partial X_i}{\partial s_j}$ and $\mathbf{x} = \mathbf{X}(\mathbf{s},t)$ is the deformation map at time t [2].

Recall that the first Piola–Kirchoff stress tensor $\mathbb{P}$ is the stress per unit *undeformed* area. It is related to the Cauchy stress by the following identity

$$\int_{\partial V} \sigma^e d\mathbf{A} = \int_{\partial V_0} \mathbb{P} d\mathbf{A}_0 \tag{3}$$

where $V = \mathbf{X}(V_0, t)$ is the image of V_0 under the deformation $\mathbf{X}(\mathbf{s}, t)$ at time t [2].

Eq. (3) and the divergence theorem imply that

$$\nabla_{\mathbf{x}} \cdot \sigma^e(\mathbf{x}, t) = \frac{1}{J(\mathbf{X}^{-1}(\mathbf{x}, t), t)} (\nabla_{\mathbf{s}} \cdot \mathbb{P})(\mathbf{X}^{-1}(\mathbf{x}, t), t) \tag{4}$$

where $\mathbf{s} = \mathbf{X}^{-1}(\mathbf{x}, t)$ is the inverse of $\mathbf{x} = \mathbf{X}(\mathbf{s}, t)$ at time t and

$$J = \det \mathbb{F} \tag{5}$$

is the Jacobian of the transformation $\mathbf{x} = \mathbf{X}(\mathbf{s}, t)$. In our notation, $\nabla_{\mathbf{x}} \cdot \sigma^e$ is a vector and each component of the vector is defined as

$$(\nabla_{\mathbf{x}} \cdot \sigma^e)_i = \sum_{j=1}^{3} \frac{\partial \sigma^e_{ij}}{\partial x_j} \tag{6}$$

Hyperelasticity [2] implies that the constitutive law for $\mathbb{P}$ is given by

$$\mathbb{P} = \frac{\partial W}{\partial \mathbb{F}} \tag{7}$$

In component form, we have

$$\mathbb{P}_{ij} = \frac{\partial W}{\partial \mathbb{F}_{ij}} \tag{8}$$

The energy associated with W is given by

$$E[\mathbf{X}] = \int_{\Omega_0} W(\mathbb{F}) d\mathbf{s} \tag{9}$$

where Ω_0 is the domain for the material coordinates and the reference configuration of the material. Here we have hidden the dependence of $\mathbb{F}$ on $\mathbf{x} = \mathbf{X}(\mathbf{s}, t)$ and therefore on the material coordinates $\mathbf{s}$.

Define the following force in terms of the variational derivative of the energy

$$\mathbf{F}(\mathbf{s}, t) = -\frac{\delta E}{\delta \mathbf{X}}(\mathbf{s}, t) \tag{10}$$

The variational derivative $\frac{\delta E}{\delta \mathbf{X}}$ is defined as follows. Consider a perturbation $\delta\mathbf{X} = \delta\mathbf{X}(\mathbf{s})$. To be called a perturbation, $\delta\mathbf{X}$ must satisfy certain smoothness properties and boundary conditions; these conditions depend on the particular problem. In elasticity, $\delta\mathbf{X}$ is usually a function in H^2 and it either satisfies Dirichlet or periodic boundary conditions. Notice that the perturbation is not a function of time. Let $\alpha \in \mathbb{R}$. Then $\phi_{\delta\mathbf{X}}(\alpha) = E[\mathbf{X} + \alpha\delta\mathbf{X}]$ is a function of α for a given deformation $\mathbf{X}$ and perturbation $\delta\mathbf{X}$. The variational derivative $\frac{\delta E}{\delta \mathbf{X}}$ is the function which satisfies the equation

$$\left.\frac{d\phi_{\delta\mathbf{X}}}{d\alpha}\right|_{\alpha=0} = \int_{\Omega_0} \frac{\delta E}{\delta \mathbf{X}}(\mathbf{s}, t) \cdot \delta\mathbf{X}(\mathbf{s}) d\mathbf{s} \tag{11}$$

for all allowed perturbations $\delta\mathbf{X}$.

Typically, $\frac{\delta E}{\delta \mathbf{X}}$ can be computed by first calculating the derivatives $\frac{d\phi_{\delta\mathbf{X}}}{d\alpha}|_{\alpha=0}$ for a general $\delta\mathbf{X}$. This results in integrals which involve derivatives in $\delta\mathbf{X}$; these derivatives can be removed by performing integration by parts. Applying the boundary conditions will give an expression of the form $\int_{\Omega_0} \frac{\delta E}{\delta \mathbf{X}}(\mathbf{s}, t) \cdot \delta\mathbf{X}(\mathbf{s}) d\mathbf{s}$.

$\mathbf{F}(\mathbf{s}, t)$ represents the force per unit *undeformed* volume. In order to compare it with $\nabla_{\mathbf{x}} \cdot \sigma^e$ we need the force per unit *deformed* volume. Let $\mathbf{f}(\mathbf{x}, t)$ describe this force density. Then $\mathbf{f}(\mathbf{x}, t)$ is defined by the equation

$$\int_V \mathbf{f}(\mathbf{x}, t) d\mathbf{x} = \int_{V_0} \mathbf{F}(\mathbf{s}, t) d\mathbf{s} \tag{12}$$

in which V_0 is an arbitrary region in the undeformed configuration. V is defined as in (3).

Performing a change of variables we obtain

$$\int_V \mathbf{f}(\mathbf{x}, t) d\mathbf{x} = \int_V \mathbf{F}(\mathbf{X}^{-1}(\mathbf{x}, t), t) J^{-1}(\mathbf{X}^{-1}(\mathbf{x}, t), t) d\mathbf{x} \tag{13}$$

Since this equation is true for all regions V,

$$\mathbf{f}(\mathbf{x},t) = \frac{1}{J(\mathbf{X}^{-1}(\mathbf{x},t),t)}\mathbf{F}(\mathbf{X}^{-1}(\mathbf{x},t),t) \tag{14}$$

In Appendix A we show that

$$\mathbf{F} = \nabla_{\mathbf{s}} \cdot \mathbb{P} \tag{15}$$

It follows from (4) that

$$\mathbf{f} = \nabla_{\mathbf{x}} \cdot \sigma^e \tag{16}$$

This implies that we can replace $\nabla_{\mathbf{x}} \cdot \sigma^e$ with $\mathbf{f}$ to obtain a model for the elastic solid which does not involve any elastic stress tensors. (The viscous stress tensor still remains, but it will disappear when we specialize to the incompressible case, below.)

Replacing $\nabla_{\mathbf{x}} \cdot \sigma^e(\mathbf{x},t)$ with $\mathbf{f}(\mathbf{x},t) = \mathbf{F}(\mathbf{X}^{-1}(\mathbf{x},t),t)/J(\mathbf{X}^{-1}(\mathbf{x},t),t)$ in (1) gives

$$\rho\left(\frac{\partial \mathbf{v}}{\partial t} + \mathbf{v}\cdot\nabla_{\mathbf{x}}\mathbf{v}\right) = \frac{1}{J(\mathbf{X}^{-1}(\mathbf{x},t),t)}\mathbf{F}(\mathbf{X}^{-1}(\mathbf{x},t),t) + \nabla_{\mathbf{x}}\cdot\sigma^v \tag{17}$$

$$\mathbf{F}(\mathbf{s},t) = -\frac{\delta E}{\delta \mathbf{X}}(\mathbf{s},t), \quad E[\mathbf{X}] = \int_{\Omega_0} W(\mathbb{F})d\mathbf{s} \tag{18}$$

This is a model for the elastic solid which involves forces that can be calculated directly from an energy functional and contains no stress tensors for the elastic forces. Notice that the equations of motion are written in Eulerian coordinates whereas the equation for the force is described in Lagrangian coordinates.

2.1. The case of incompressible deformation

In modeling incompressible deformations, we impose the constraint of incompressibility in Eulerian form where it is a linear condition ($\nabla_{\mathbf{x}}\cdot\mathbf{v} = 0$) instead of using its nonlinear Lagrangian form $\frac{\partial J}{\partial t} = 0$, i.e., $J(\mathbf{s},t) = J(\mathbf{s})$, independent of t.

Then (17) and (18) become

$$\rho\left(\frac{\partial \mathbf{v}}{\partial t} + \mathbf{v}\cdot\nabla_{\mathbf{x}}\mathbf{v}\right) + \nabla_{\mathbf{x}}p = \frac{1}{J(\mathbf{X}^{-1}(\mathbf{x},t))}\mathbf{F}(\mathbf{X}^{-1}(\mathbf{x},t),t) + \mu\Delta_{\mathbf{x}}\mathbf{v} \tag{19}$$

$$\nabla_{\mathbf{x}}\cdot\mathbf{v} = 0 \tag{20}$$

$$\mathbf{F}(\mathbf{s},t) = -\frac{\delta E}{\delta \mathbf{X}}(\mathbf{s},t), \quad E[\mathbf{X}] = \int_{\Omega_0} W(\mathbb{F})d\mathbf{s} \tag{21}$$

where we have chosen σ^v to be the Navier–Stokes stress tensor and used incompressibility to simplify the expression for the viscous forces. The constant μ is the viscosity. Note that there are no stress tensors in this formulation, since we have chosen to write viscous stresses in Eulerian coordinates, and since we compute the elastic forces from an energy functional.

We consider the case of an isotropic elastic material. Isotropic implies that $W = W(I_1,I_2,I_3)$ where I_1,I_2,I_3 are the invariants of the right Cauchy–Green deformation tensor $\mathbb{C} = \mathbb{F}^T\mathbb{F}$ [2].

More specifically,

$$I_1 = \mathrm{tr}(\mathbb{C}) \tag{22}$$

$$I_2 = \frac{1}{2}(\mathrm{tr}(\mathbb{C})^2 - \mathrm{tr}(\mathbb{C}^2)) \tag{23}$$

$$I_3 = \det(\mathbb{C}) \tag{24}$$

In the special case that $\mathbf{X}(\mathbf{s},0) = \mathbf{s}$, we have $J \equiv 1$, which implies that $I_3 \equiv 1$.

Let

$$\widehat{W}(I_1,I_2) = W(I_1,I_2,1) \tag{25}$$

and

$$\widehat{E}[\mathbf{X}] = \int_{\Omega_0} \widehat{W}(I_1,I_2)d\mathbf{s} \tag{26}$$

In Appendix B, we prove that the difference between the Eulerian force densities corresponding to $\frac{\delta E}{\delta \mathbf{X}}$ and $\frac{\delta \widehat{E}}{\delta \mathbf{X}}$ is a gradient term. Since this difference can be incorporated into the term $\nabla_{\mathbf{x}}\,p$, the resulting motion is the same if E is replaced by $\widehat{E}$ in (21); the only difference is the calculated pressure.

It is numerically advantageous to use the simplified energy functional (26) instead of the full energy functional (9). In the 'Results' section, we comment on this briefly.

2.2. Immersed boundary formulation of model

Replacing $\nabla_{\mathbf{x}}\cdot\sigma^e(\mathbf{x},t)$ by $\mathbf{f}(\mathbf{x},t) = \mathbf{F}(\mathbf{X}^{-1}(\mathbf{x},t),t)/J(\mathbf{X}^{-1}(\mathbf{x},t),t)$ as in (19) allows us to compute the elastic forces without reference to a stress tensor, but this formulation of $\mathbf{f}$ is difficult to use in numerical computations. We are interested in computing $\mathbf{f}$ on a grid in the spatial domain. The above formula says that for each $\mathbf{x}$ in the grid, we need to compute its

corresponding material point $\mathbf{X}^{-1}(\mathbf{x},t)$ and then evaluate $\mathbf{F}$ at $\mathbf{X}^{-1}(\mathbf{x},t)$. This is a complicated procedure, which we avoid as follows.

In this subsection, our goal is to rewrite $\mathbf{f}(\mathbf{x},t)$ in terms of an explicit formula which involves $\mathbf{F}(\mathbf{s},t)$; this formula must perform an implicit change of coordinates so we do not have to compute $\mathbf{X}^{-1}(\mathbf{x},t)$. This is exactly what the immersed boundary formulation accomplishes [3].

If our interpolation formula performs a change of variables, we must write $\mathbf{f}(\mathbf{x},t)$ in terms of an integral. This can be done by introducing the Dirac delta function:

$$\mathbf{f}(\mathbf{x},t) = \int_{\Omega} \mathbf{f}(\mathbf{y},t)\delta(\mathbf{x}-\mathbf{y})d\mathbf{y} \tag{27}$$

$$= \int_{\Omega} \frac{1}{J(\mathbf{X}^{-1}(\mathbf{y},t))}\mathbf{F}(\mathbf{X}^{-1}(\mathbf{y},t),t)\delta(\mathbf{x}-\mathbf{y})d\mathbf{y} \tag{28}$$

If we perform the formal change of variables $\alpha = \mathbf{X}^{-1}(\mathbf{y},t)$ then we obtain

$$\mathbf{f}(\mathbf{x},t) = \int_{\Omega_0} \mathbf{F}(\alpha,t)\delta(\mathbf{x}-\mathbf{X}(\alpha,t))d\alpha \tag{29}$$

This is the immersed boundary recipe for the evaluation of $\mathbf{f}(\mathbf{x},t)$. Neither the Jacobian J nor the inverse coordinate transformation $s = \mathbf{X}^{-1}(\mathbf{x},t)$ appears in (29).

Note that the integration variable α appears nonlinearly in the argument of the delta function through $\mathbf{X}(\alpha,t)$. Thus, the numerical values of $\mathbf{f}$ and $\mathbf{F}$ are *not* the same at corresponding points. Instead, $\mathbf{f}$ and $\mathbf{F}$ are corresponding densities. (Their numerical values do coincide at corresponding points, however, in the special case $J \equiv 1$.)

Using the above formulation for $\mathbf{f}(\mathbf{x},t)$ we can rewrite (19)–(21) as

$$\rho\left(\frac{\partial \mathbf{v}}{\partial t} + \mathbf{v}\cdot\nabla_{\mathbf{x}}\mathbf{v}\right) + \nabla_{\mathbf{x}}p = \int_{\Omega_0} \mathbf{F}(\mathbf{s},t)\delta(\mathbf{x}-\mathbf{X}(\mathbf{s},t))d\mathbf{s} + \mu\Delta_{\mathbf{x}}\mathbf{v} \tag{30}$$

$$\nabla_{\mathbf{x}}\cdot\mathbf{v} = 0 \tag{31}$$

$$\mathbf{F}(\mathbf{s},t) = -\frac{\delta E}{\delta \mathbf{X}}(\mathbf{s},t), \quad E[\mathbf{X}] = \int_{\Omega_0} W(\mathbb{F})d\mathbf{s} \tag{32}$$

In the system described by Eqs. (30)–(32), $\mathbf{v}(\mathbf{x},t)$, $p(\mathbf{x},t)$, and $\mathbf{X}(\mathbf{s},t)$ are the unknowns. This is a system with 4 equations and 7 unknowns (counting the components of $\mathbf{v}$ and $\mathbf{X}$). To complete the system we append the 3 equations

$$\frac{\partial \mathbf{X}}{\partial t}(\mathbf{s},t) = \mathbf{v}(\mathbf{X}(\mathbf{s},t),t) \tag{33}$$

which is simply the definition of the velocity field $\mathbf{v}$. We also assume periodic boundary conditions for the velocity field.

The complete system of equations is given by

$$\rho\left(\frac{\partial \mathbf{v}}{\partial t} + \mathbf{v}\cdot\nabla_{\mathbf{x}}\mathbf{v}\right) + \nabla_{\mathbf{x}}p = \mu\Delta_{\mathbf{x}}\mathbf{v} + \mathbf{f} \tag{34}$$

$$\nabla_{\mathbf{x}}\cdot\mathbf{v} = 0 \tag{35}$$

$$\mathbf{f}(\mathbf{x},t) = \int_{\Omega_0} \mathbf{F}(\mathbf{s},t)\delta(\mathbf{x}-\mathbf{X}(\mathbf{s},t))d\mathbf{s} \tag{36}$$

$$\mathbf{F}(\mathbf{s},t) = -\frac{\delta E}{\delta \mathbf{X}}(\mathbf{s},t), \quad E[\mathbf{X}] = \int_{\Omega_0} W(\mathbb{F})d\mathbf{s} \tag{37}$$

$$\frac{\partial \mathbf{X}}{\partial t}(\mathbf{s},t) = \mathbf{v}(\mathbf{X}(\mathbf{s},t),t) = \int_{\Omega} \mathbf{v}(\mathbf{x},t)\delta(\mathbf{x}-\mathbf{X}(\mathbf{s},t))d\mathbf{x} \tag{38}$$

Note that the second equality in (38) is just the defining property of the Dirac delta function. We include this version of (38) here because it will become useful when we discretize the above system.

We call this the immersed boundary formulation of incompressible viscoelasticity, even though there is no immersed boundary in the problem we are considering. The reason for this terminology is that we are using the mathematical apparatus of the immersed boundary method, see [3].

Note the duality between (36) and (38), both of which involve conversions between Lagrangian and Eulerian variables. These conversions are accomplished by integral transformations in which the Dirac delta function appears as a kernel.

3. Discretization of the model

In this section, we present a discretization of Eqs. (34)–(38). First, we describe a method for approximating the Lagrangian force density $\mathbf{F}(\mathbf{s},t)$. Then we discuss a discretization of the interaction equations ((36) and (38)), a discretization of the

spatial differential operators in the equations of motion, and an approximation to the delta function. Finally, we present a temporal discretization of the spatially discretized system.

3.1. Computational meshes

In this subsection, we will describe the meshes used in the discretization of the system. We take $\Omega_0 = [0,2\pi]^d$, where $d = 2$ or 3, as the reference configuration of the material. Ω_0 is discretized using a triangular mesh in two dimensions and a tetrahedral mesh in three dimensions. The elastic forces are computed at the vertices of each element. (In the following, we refer to the vertices as finite element nodes.) The positions of these vertices in the reference configuration are denoted by $\mathbf{s}^{(1)}, \mathbf{s}^{(2)}, \ldots, \mathbf{s}^{(N_v)}$; in the deformed configuration, they are denoted by $\mathbf{X}^{(1)}, \mathbf{X}^{(2)}, \ldots, \mathbf{X}^{(N_v)}$. In the following, we will focus on the three-dimensional case. The two-dimensional case is similar.

In our discretization, we use finite differences on a staggered grid to solve the Eulerian equations of motion [4]. We take the domain for the spatial coordinates to be $\Omega = [0,2\pi]^3$.

Let

$$g_1^h = \left\{ \left(ih, \left(j+\frac{1}{2}\right)h, \left(k+\frac{1}{2}\right)h \right),\ i,j,k = 0,\ldots,N-1 \right\} \tag{39}$$

$$g_2^h = \left\{ \left(\left(i+\frac{1}{2}\right)h, jh, \left(k+\frac{1}{2}\right)h \right),\ i,j,k = 0,\ldots,N-1 \right\} \tag{40}$$

$$g_3^h = \left\{ \left(\left(i+\frac{1}{2}\right)h, \left(j+\frac{1}{2}\right)h, kh \right),\ i,j,k = 0,\ldots,N-1 \right\} \tag{41}$$

$$g_c^h = \left\{ \left(\left(i+\frac{1}{2}\right)h, \left(j+\frac{1}{2}\right)h, \left(k+\frac{1}{2}\right)h \right),\ i,j,k = 0,\ldots,N-1 \right\} \tag{42}$$

The velocity component v_α is defined on the grid g_α^h and the pressure p is defined on g_c^h. We refer to this staggered grid as the Eulerian grid.

3.2. Lagrangian force computations

Given a tetrahedral mesh for the reference configuration, we approximate the deformation $\mathbf{x} = \mathbf{X}(\mathbf{s},t)$ by a linear function on each tetrahedron T. We denote the overall piecewise linear function by $\widetilde{\mathbf{X}}$.

In particular,

$$\widetilde{X}_i(\mathbf{s},t)|_T = \sum_{j=1}^{3} a_{ij} s_j + b_i \tag{43}$$

Note that if $\mathbf{X}^{(k_0)}(t)$, $\mathbf{X}^{(k_1)}(t)$, $\mathbf{X}^{(k_2)}(t)$, and $\mathbf{X}^{(k_3)}(t)$ are the positions of the vertices of tetrahedron T at time t then each a_{ij} is determined by these four vectors.

Applying the energy functional E to the deformation $\widetilde{\mathbf{X}}$ gives $E[\widetilde{\mathbf{X}}]$, which depends on a_{ij} and therefore on $\mathbf{X}^{(k)}$, $k = 1,\ldots,N_v$. That is,

$$E[\widetilde{\mathbf{X}}] = \widetilde{E}(\mathbf{X}^{(1)},\ldots,\mathbf{X}^{(N_v)})$$

Note that $\widetilde{E}(\mathbf{X}^{(1)},\ldots,\mathbf{X}^{(N_v)})$ is the exact elastic energy of the piecewise linear deformation with vertices $\mathbf{X}^{(1)},\ldots,\mathbf{X}^{(N_v)}$.

Recall that $\mathbf{F}(\mathbf{s},t) = -\frac{\delta E}{\delta \mathbf{X}}(\mathbf{s},t)$; that is, the Lagrangian force density is the variational derivative of the energy functional. Analogously, we define

$$\mathbf{F}^{(k)} = -\frac{\partial \widetilde{E}}{\partial \mathbf{X}^{(k)}} \tag{44}$$

Here, $\frac{\partial \widetilde{E}}{\partial \mathbf{X}^{(k)}}$ denotes the gradient of $\widetilde{E}$ with respect to $\mathbf{X}^{(k)}$, that is,

$$\left(\frac{\partial \widetilde{E}}{\partial \mathbf{X}^{(k)}} \right)_l = \frac{\partial \widetilde{E}}{\partial X_l^{(k)}}$$

for $l = 1,2,3$. The derivatives $\partial \widetilde{E}/\partial \mathbf{X}^{(k)}$ are calculated analytically, not numerically (see below).

We take $\mathbf{F}^{(k)}$ as the force at the kth finite element node. We point out that $\mathbf{F}^{(k)}$ is a force and not a force density. Thus, as $N_v \to \infty$ and the meshwidth of the tetrahedral mesh goes to zero, $\mathbf{F}^{(k)} \to 0$ for each k. The sum of the $\mathbf{F}^{(k)}$ over all nodes k that fall within a fixed region of space at some given time has a finite limit as $N_v \to \infty$, however.

In order to compute $\mathbf{F}^{(k)}$, we compute the force at node k contributed by each individual tetrahedron T, and then add up these forces over all of the tetrahedra that touch node k.

In particular, let

$$E_T[\mathbf{X}] = \int_T W(\mathbb{F}) d\mathbf{s} \tag{45}$$

and

$$\widetilde{E}_T(\mathbf{X}^{(1)},\ldots,\mathbf{X}^{(N_v)}) = E_T[\widetilde{\mathbf{X}}] \tag{46}$$

Then $\widetilde{E}_T$ is the elastic energy contributed by tetrahedron T. Although we have written $\widetilde{E}_T$ as a function of $\mathbf{X}^{(k)}$, $k = 1,\ldots,N_v$, notice that $\widetilde{E}_T$ is only a function of the current positions of the four vertices of T.

Then

$$\mathbf{F}_T^{(k)} = -\frac{\partial \widetilde{E}_T}{\partial \mathbf{X}^{(k)}} \tag{47}$$

is the force at node k contributed by an individual tetrahedron.

To compute $\mathbf{F}_T^{(k)}$, we use the fact that $\widetilde{\mathbf{X}}$ is linear when restricted to a tetrahedron. Then

$$\mathbb{F}_{ij} = \frac{\partial \widetilde{X}_i}{\partial s_j} = a_{ij} \tag{48}$$

by Eq. (43). Using Eqs. (45) and (46), we can write

$$\widetilde{E}_T = \int_T W(\ldots,a_{ij},\ldots)d\mathbf{s} \tag{49}$$

The transformation entries a_{ij}, $i,j = 1,\ldots,3$, are constant for each tetrahedron, so we can trivially evaluate the integral in (49) exactly:

$$\widetilde{E}_T = W(\ldots,a_{ij},\ldots)V_{\mathrm{ref}}(T) \tag{50}$$

where $V_{\mathrm{ref}}(T)$ denotes the volume of T in the reference configuration.

Thus,

$$\mathbf{F}_T^{(k)} = -\sum_{i,j=1}^{3} \frac{\partial W}{\partial a_{ij}} \frac{\partial a_{ij}}{\partial \mathbf{X}^{(k)}} V_{\mathrm{ref}}(T) \tag{51}$$

Formulae for the $\partial a_{ij}/\partial \mathbf{X}^{(k)}$ in terms of the positions of the vertices of T in the deformed configuration can be found in Appendix C.

Note that if node k is not a vertex of T then the a_{ij} do not depend on $\mathbf{X}^{(k)}$, and, therefore, $\mathbf{F}_T^{(k)} = 0$. Consequently, we need only calculate $\mathbf{F}_T^{(k)}$ for the nodes on T. Also, note that only the formula for $\partial W/\partial a_{ij}$ changes if the material model changes. The formulae for $\partial a_{ij}/\partial \mathbf{X}^{(k)}$, and therefore the code that evaluates these formulae, are independent of the choice of the stored energy potential W. This makes it easy to switch from one material model to another.

To compute $\mathbf{F}^{(k)}$ from $\mathbf{F}_T^{(k)}$, we use the identity

$$\mathbf{F}^{(k)} = \sum_T \mathbf{F}_T^{(k)} \tag{52}$$

Since $\mathbf{F}_T^{(k)}$ depends only on the configuration of tetrahedron T, we can compute the $\mathbf{F}_T^{(k)}$ in parallel.

The procedure for computing $\mathbf{F}^{(k)}$ via $\mathbf{F}_T^{(k)}$ is similar to assembling stiffness matrices in finite element computations. For each T, we first compute $\mathbf{F}_T^{(k_0)}$, $\mathbf{F}_T^{(k_1)}$, $\mathbf{F}_T^{(k_2)}$, $\mathbf{F}_T^{(k_3)}$, where k_0, k_1, k_2, and k_3 denote the indices of the nodes of T, and then add these contributions to the global force vectors $\mathbf{F}^{(k_0)}$, $\mathbf{F}^{(k_1)}$, $\mathbf{F}^{(k_2)}$, $\mathbf{F}^{(k_3)}$. In this procedure, we need only know which vertices belong to a particular tetrahedron, rather than which tetrahedra touch a particular node. Although the tetrahedral mesh used in the present paper was constructed by hand, automatic mesh generators typically provide the needed information. Note that unlike finite element computations, our method does not use shape functions in our force computations, and we do not solve a linear system involving the mass matrix.

3.3. Discretization of interaction equations

In this subsection, we present a discretization of Eqs. (36) and (38). Let $\delta_h(\mathbf{x})$ be an approximation to the delta function $\delta(\mathbf{x})$ (which is defined for all $\mathbf{x} \in \mathbb{R}^3$). (There are different choices for approximating the delta function. We will mention our recommendation in a later subsection.)

Recall the interaction equations for the velocity field and Eulerian force density:

$$\mathbf{v}(\mathbf{X}(\mathbf{s},t),t) = \int_\Omega \mathbf{v}(\mathbf{x},t)\delta(\mathbf{x}-\mathbf{X}(\mathbf{s},t))d\mathbf{x} \tag{53}$$

$$\mathbf{f}(\mathbf{x},t) = \int_{\Omega_0} \mathbf{F}(\mathbf{s},t)\delta(\mathbf{x}-\mathbf{X}(\mathbf{s},t))d\mathbf{s} \tag{54}$$

We use the trapezoidal rule (on our periodic domain) to discretize (53)

$$v_\alpha(\mathbf{X}(\mathbf{s},t),t) = \sum_{\mathbf{x}\in g_\alpha^h} v_\alpha(\mathbf{x},t)\delta_h(\mathbf{x}-\mathbf{X}(\mathbf{s},t))h^3 \tag{55}$$

Notice that this is an interpolation formula for computing v_α at an arbitrary point $\mathbf{X}(\mathbf{s},t)$ given v_α on the equally spaced grid g^h_α [3].

We discretize (54) in a manner similar to (53)

$$f_\alpha(\mathbf{x},t) = \sum_{k=1}^{N_\nu} F^{(k)}_\alpha \delta_h(\mathbf{x} - \mathbf{X}^{(k)}) \quad \text{for all } \mathbf{x} \in g^h_\alpha \tag{56}$$

where

$$\mathbf{F}^{(k)} = -\frac{\partial \widetilde{E}}{\partial \mathbf{X}^{(k)}} \tag{57}$$

Since $\mathbf{F}^{(k)}$ is a force and not a force density, there is no need to attribute a specific volume to the kth finite element node. Note in particular the absence of any factor corresponding to $d\mathbf{s}$ in (56). This is because $\mathbf{F}^{(k)}$ as defined by (57) is already $O(d\mathbf{s})$.

3.4. Discretization of Eulerian equations

Now we discuss a discretization of the spatial differential operators in the equations of motion. First, we rewrite the equations of motion to put the convection term into a skew-symmetric form. Since $\nabla_{\mathbf{x}} \cdot \mathbf{v} = 0$ we have the identity

$$\mathbf{v} \cdot \nabla_{\mathbf{x}} \phi = \frac{1}{2}\mathbf{v} \cdot \nabla_{\mathbf{x}} \phi + \frac{1}{2}\nabla_{\mathbf{x}} \cdot (\mathbf{v}\phi) \tag{58}$$

for all scalar-valued functions ϕ.

In component form, the equations of motion become

$$\rho\left(\frac{\partial v_\alpha}{\partial t} + \frac{1}{2}\mathbf{v} \cdot \nabla_{\mathbf{x}} v_\alpha + \frac{1}{2}\nabla_{\mathbf{x}} \cdot (\mathbf{v} v_\alpha)\right) + \frac{\partial p}{\partial x_\alpha} = \mu \Delta_{\mathbf{x}} v_\alpha + \int_{\Omega_0} F_\alpha(\mathbf{s},t)\delta(\mathbf{x} - \mathbf{X}(\mathbf{s},t))d\mathbf{s} \tag{59}$$

for each $\alpha = 1,2,3$, together with the constraint

$$\nabla_{\mathbf{x}} \cdot \mathbf{v} = 0 \tag{60}$$

This form is essential for deriving the viscous decay of the energy in the spatially discretized case. (See [3] for more details.) Let

$$D^h_\alpha \phi := \frac{\phi\left(\mathbf{x} + \frac{h}{2}\mathbf{e}_\alpha\right) - \phi\left(\mathbf{x} - \frac{h}{2}\mathbf{e}_\alpha\right)}{h}, \quad \alpha = 1,2,3 \tag{61}$$

be the central difference approximation to the first order partial derivative $\frac{\partial}{\partial x_\alpha}$. Here, $\mathbf{e}_1$, $\mathbf{e}_2$, $\mathbf{e}_3$ are the standard basis vectors.

Notice that $D^h_\alpha \phi$ is not defined on the same grid as ϕ. For example, if ϕ is defined on g^h_c then $D^h_\alpha \phi$ is defined on g^h_α. The function $D^{2h}_\alpha \phi$ is defined, however, on the same grid as ϕ.

We take

$$\mathbf{D}^h := \left(D^h_1, D^h_2, D^h_3\right) \tag{62}$$

as a discretization to the gradient operator.

Let

$$L^h \phi := \sum_{\alpha=1}^{3} \frac{\phi(\mathbf{x} + h\mathbf{e}_\alpha) - 2\phi(\mathbf{x}) + \phi(\mathbf{x} - h\mathbf{e}_\alpha)}{h^2} \tag{63}$$

be the central difference approximation to the Laplacian operator. $L^h\phi$ is defined on the same grid as ϕ, and this can be any of the grids g^h_α.

Next, let $S(\mathbf{v})\phi$ denote the discretization to $\frac{1}{2}\mathbf{v} \cdot \nabla_{\mathbf{x}} \phi + \frac{1}{2}\nabla_{\mathbf{x}}(\mathbf{v}\phi)$. To define this discretization we need the operator

$$I^h_{\beta\to\alpha}\phi(\mathbf{x}) := \sum_{\mathbf{y} \in g^h_\beta} \phi(\mathbf{y})\delta_h(\mathbf{y} - \mathbf{x})h^3 \tag{64}$$

where $x \in g^h_\alpha$. Note that $I^h_{\beta\to\alpha}$ defines an interpolation operator from functions defined on g^h_β to functions defined on g^h_α. Then we define, with the help of the above interpolation operator,

$$S(\mathbf{v})v_\alpha = \frac{1}{2}\sum_{\beta=1}^{3}\left(\left(I^h_{\beta\to\alpha} v_\beta\right) D^{2h}_\beta v_\alpha + D^{2h}_\beta\left(\left(I^h_{\beta\to\alpha} v_\beta\right) v_\alpha\right)\right) \tag{65}$$

Notice that $S(\mathbf{v})v_\alpha$ is defined on g^h_α. The operator $I^h_{\beta\to\alpha}$ is used to define the velocity $\mathbf{v}$ that appears in the operator $S(\mathbf{v})$. This means that we use the same interpolation scheme to construct the convection velocity $\mathbf{v}$ as we do to evaluate the velocity that is used to move the finite element nodes.

Using these difference operators, (55) and (56), the spatially discretized system becomes

$$\rho\left(\frac{dv_\alpha}{dt}+S(\mathbf{v})v_\alpha\right)+D_\alpha^h p=\mu L^h v_\alpha+f_\alpha \quad \text{for all } \mathbf{x}\in g_\alpha^h \tag{66}$$

$$\mathbf{D}^h\cdot\mathbf{v}=0 \quad \text{for all } \mathbf{x}\in g_c^h \tag{67}$$

$$f_\alpha(\mathbf{x},t)=-\sum_{k=1}^{N_v}\frac{\partial\widetilde{E}}{\partial\mathbf{X}^{(k)}}\delta_h(\mathbf{x}-\mathbf{X}^{(k)}) \quad \text{for all } \mathbf{x}\in g_\alpha^h \tag{68}$$

$$\frac{dX_\alpha^{(k)}}{dt}=\sum_{\mathbf{x}\in g_\alpha^h}v_\alpha(\mathbf{x},t)\delta_h(\mathbf{x}-\mathbf{X}^{(k)})h^3 \tag{69}$$

3.5. Discretization of the delta function

In the numerical simulations of this paper, the following discretization was used for the delta function:

$$\delta_h(\mathbf{x}):=\frac{1}{h^3}\phi\left(\frac{x}{h}\right)\phi\left(\frac{y}{h}\right)\phi\left(\frac{z}{h}\right)$$

where $\phi(r)$ is defined as

$$\phi(r)=\begin{cases}\frac{1}{8}\left(3-2|r|+\sqrt{1+4|r|-4|r|^2}\right) & \text{for all } 0\leqslant|r|\leqslant 1\\ \frac{1}{8}\left(5-2|r|-\sqrt{-7+12|r|-4|r|^2}\right) & \text{for all } 1\leqslant|r|\leqslant 2\\ 0 & \text{for all } |r|\geqslant 2\end{cases} \tag{70}$$

A discussion of the motivation for this discretization can be found in [3].

3.6. Temporal discretization

We now discuss a second-order temporal discretization of the spatially discretized system given by (66)–(69) [3]. The timestepping scheme will be based on the following second-order Runge–Kutta method.

Let

$$\mathbf{y}'(t)=\mathbf{f}(t,\mathbf{y}) \tag{71}$$

Then the second-order Runge–Kutta method is given by two steps:

Step 1:

$$\mathbf{y}^{n+\frac{1}{2}}=\mathbf{y}^n+\frac{\Delta t}{2}\mathbf{f}(t_n,\mathbf{y}^n) \tag{72}$$

Step 2:

$$\mathbf{y}^{n+1}=\mathbf{y}^n+\Delta t\mathbf{f}\left(t_{n+\frac{1}{2}},\mathbf{y}^{n+\frac{1}{2}}\right) \tag{73}$$

where $\mathbf{y}^n$ is the approximation to $\mathbf{y}(t_n)$.

Our timestepping scheme for (66)–(69) is a modification of the foregoing Runge–Kutta method. (The equations are stated here, and the specific order in which they are used will be explained later.)

Step 1:

$$\rho\left(\frac{v_\alpha^{n+\frac{1}{2}}-v_\alpha^n}{\frac{\Delta t}{2}}+S(\mathbf{v}^n)v_\alpha^n\right)+D_\alpha^h p^{n+\frac{1}{2}}=\mu L^h v_\alpha^{n+\frac{1}{2}}+f_\alpha^{n+\frac{1}{2}} \quad \text{for all } \mathbf{x}\in g_\alpha^h \tag{74}$$

$$\mathbf{D}^h\cdot\mathbf{v}^{n+\frac{1}{2}}=0 \quad \text{for all } \mathbf{x}\in g_c^h \tag{75}$$

$$f_\alpha^{n+\frac{1}{2}}(\mathbf{x})=-\sum_{k=1}^{N_v}\frac{\partial\widetilde{E}}{\partial\mathbf{X}^{(k)}}\left(\ldots,\mathbf{X}^{(l)}\left(t_{n+\frac{1}{2}}\right),\ldots\right)\delta_h\left(\mathbf{x}-\mathbf{X}^{(k)}\left(t_{n+\frac{1}{2}}\right)\right) \quad \text{for all } \mathbf{x}\in g_\alpha^h \tag{76}$$

$$\frac{X_\alpha^{(k)}\left(t_{n+\frac{1}{2}}\right)-X_\alpha^{(k)}(t_n)}{\frac{\Delta t}{2}}=\sum_{\mathbf{x}\in g_\alpha^h}v_\alpha^n(\mathbf{x})\delta_h(\mathbf{x}-\mathbf{X}^{(k)}(t_n))h^3 \tag{77}$$

Step 2:

$$\rho\left(\frac{v_\alpha^{n+1}-v_\alpha^n}{\Delta t}+S\left(\mathbf{v}^{n+\frac{1}{2}}\right)v_\alpha^{n+\frac{1}{2}}\right)+D_\alpha^h\tilde{p}^{n+\frac{1}{2}}=\mu L^h\left(\frac{1}{2}\left(v_\alpha^n+v_\alpha^{n+1}\right)\right)+f_\alpha^{n+\frac{1}{2}}\quad\text{for all } \mathbf{x}\in g_\alpha^h \tag{78}$$

$$\mathbf{D}^h\cdot\mathbf{v}^{n+1}=0\quad\text{for all } \mathbf{x}\in g_c^h \tag{79}$$

$$\frac{X_\alpha^{(k)}(t_{n+1})-X_\alpha^{(k)}(t_n)}{\Delta t}=\sum_{\mathbf{x}\in g_\alpha^h}v_\alpha^{n+\frac{1}{2}}(\mathbf{x})\delta_h\left(\mathbf{x}-\mathbf{X}^{(k)}\left(t_{n+\frac{1}{2}}\right)\right)h^3 \tag{80}$$

Here, $\mathbf{v}^n(\mathbf{x})$ is the approximation to the velocity $\mathbf{v}(\mathbf{x},t_n)$ and $\mathbf{X}^{(k)}(t_n)$ is the approximation to the deformation $\mathbf{X}(\mathbf{s}^{(k)},t_n)$. Similar notation is used for the other variables. Both $p^{n+\frac{1}{2}}$ and $\tilde{p}^{n+\frac{1}{2}}$ produce approximations to p at $t_{n+\frac{1}{2}}$; they may be different since they are byproducts of solving different linear systems.

In the standard second-order Runge–Kutta scheme, all of the terms are treated explicitly in the first step; in our discretization of the equations of motion, we instead treat the $\mathbf{D}^h p$ and $L^h\mathbf{v}$ terms implicitly by evaluating them at the $(n+1/2)$ timestep rather than the nth timestep. In the second step, we use the Crank–Nicolson scheme on the diffusion term $L^h\mathbf{v}$. Both of these modifications improve stability.

The basic procedure for solving the discretized equations at each time step (having computed $\mathbf{v}^n$, $\mathbf{X}^{(k)}(t_n)$ at the previous timestep) is as follows:

Step 1:

1. Compute $\mathbf{X}^{(k)}\left(t_{n+\frac{1}{2}}\right)$ via (77).
2. Use $\mathbf{X}^{(k)}\left(t_{n+\frac{1}{2}}\right)$ to compute $\mathbf{f}^{n+\frac{1}{2}}$ via (76).
3. Solve (see below) the equations of motion given by (74) and (75) to compute $\mathbf{v}^{n+\frac{1}{2}}$ and $p^{n+\frac{1}{2}}$.

Step 2:

1. Using $\mathbf{f}^{n+\frac{1}{2}}$ from Step 1, solve (see below) the equations of motion given by (78) and (79) to compute $\mathbf{v}^{n+1}$ and $\tilde{p}^{n+\frac{1}{2}}$.
2. Use $\mathbf{v}^{n+\frac{1}{2}}$ and $\mathbf{X}^{(k)}(t_{n+\frac{1}{2}})$ from Step 1 (as well as $\mathbf{X}^{(k)}(t_n)$) to compute $\mathbf{X}^k(t_{n+1})$ via (80).

Notice that the order of the substeps in Step 2 does not matter (since they are independent of each other). Also, the force $\mathbf{f}^{n+\frac{1}{2}}$ only needs to be computed once in Step 1. One might wonder why we bother to compute the velocity field $\mathbf{v}^{n+1}$, since it is not used in the update of the position variables $\mathbf{X}^{(k)}$. It is, however, used in the next timestep, where it plays the role of $\mathbf{v}^n$.

Eqs. (74) and (75) in Step 1 and (78) and (79) in Step 2 each result in a $4N^3\times 4N^3$ linear system that needs to be solved. In both steps, the linear system can be written in the form

$$\left(I-\frac{\mu\Delta t}{2\rho}L^h\right)v_\alpha+D_\alpha^h q=w_\alpha\quad\text{for all } \mathbf{x}\in g_\alpha^h \tag{81}$$

$$\mathbf{D}^h\cdot\mathbf{v}=0\quad\text{for all } \mathbf{x}\in g_c^h \tag{82}$$

where, in Step 1,

$$v_\alpha=v_\alpha^{n+\frac{1}{2}},\quad q=\frac{\Delta t}{2\rho}p^{n+\frac{1}{2}},\quad w_\alpha=v_\alpha^n-\frac{\Delta t}{2}S(\mathbf{v}^n)v_\alpha^n+\frac{\Delta t}{2\rho}f_\alpha^{n+\frac{1}{2}} \tag{83}$$

and, in Step 2,

$$v_\alpha=v_\alpha^{n+1},\quad q=\frac{\Delta t}{\rho}\tilde{p}^{n+\frac{1}{2}},\quad w_\alpha=v_\alpha^n-\Delta tS\left(\mathbf{v}^{n+\frac{1}{2}}\right)v_\alpha^{n+\frac{1}{2}}+\frac{\mu\Delta t}{2\rho}L^h v_\alpha^n+\frac{\Delta t}{\rho}f_\alpha^{n+\frac{1}{2}} \tag{84}$$

Since v_α and q are periodic and defined on uniform grids, the Discrete Fourier Transform (DFT) can be used to solve the linear systems. It would be complicated, however, to apply the DFT directly to (81) since each of the v_α and q are defined on different grids. Instead, we first apply the discrete divergence operator to Eq. (81) to obtain an equation for q:

$$L^h q=\mathbf{D}^h\cdot\mathbf{w} \tag{85}$$

Here, we have made use of two operator identities: $\mathbf{D}^h\cdot\mathbf{D}^h=L^h$ and $D_\alpha^h L^h=L^h D_\alpha^h$. The first identity follows from Eqs. (61)–(63) and the second identity is true because we have periodic boundary conditions.

Eq. (85) is an $N^3\times N^3$ linear system in which q, $L^h q$, and $\mathbf{D}^h\cdot\mathbf{w}$ are all defined on the grid g_c^h. Application of the DFT to this system reduces it to N^3 scalar equations that can be solved in parallel. Application of an inverse DFT then yields the solution q. With q known, we have three separate linear systems, one for each of the v_α:

$$\left(I-\frac{\mu\Delta t}{2\rho}L^h\right)v_\alpha=w_\alpha-D_\alpha^h q \tag{86}$$

Each of these linear systems is defined on its own grid g_α^h and can be solved by DFT for v_α in the same manner as Eq. (85) was solved for q, as described above.

4. Numerical results

4.1. 2D results

In this subsection, we present our two-dimensional results. We apply the method to a warm-up problem in which an incompressible viscoelastic material fills a periodic domain. The elastic material is initially undeformed but has a nonzero initial velocity. It deforms under this velocity, generating elastic forces that result in a damped oscillation around the undeformed reference configuration.

As described in Section 3, a staggered grid is used to discretize the spatial domain and a triangular mesh to discretize the reference configuration of the material. We generated a coarse triangular mesh on our $2\pi \times 2\pi$ periodic domain in the following way. First we generated a Cartesian grid of points on this domain with meshwidth $h_c = 2\pi/64$. Next, we randomly moved each point on the grid except for the corners of the domain. Each point was allowed to move at most a distance of $\beta_{2D}h_c$ in each direction where β_{2D} was chosen to prevent thin or poorly shaped elements. We used $\beta_{2D} = 0.3$. In constructing the mesh, the points on the boundary were constrained to stay on the boundary, but they were allowed to move along a boundary edge. The set of perturbed grid points was fed into Matlab's Delaunay Triangulation function to create a triangular mesh with effective meshwidth close to h_c. To refine the coarse mesh, each triangle was divided into four new triangles by connecting the midpoints of the edges; this divides the effective meshwidth by two.

In our simulations, the coarse triangular mesh described above, which has 64^2 nodes, is used in conjunction with a 32×32 Cartesian grid for the Eulerian variables. Thus, the triangular mesh has half the effective meshwidth, and four times the number of nodes, as its Eulerian counterpart. These relationships are maintained as we do mesh refinement.

We studied the warm-up problem described previously with two elastic energy functionals. Both of the energy functionals are first formulated in three dimensions. The two-dimensional case is then derived by assuming there is no deformation in the third dimension (the deformation is planar) and the displacement $\mathbf{u} = \mathbf{X} - \mathbf{s}$ does not depend on s_3 so the deformation in each cross-section perpendicular to the third dimension is the same. That is, we assume $X_3 = s_3$, $X_1 = X_1(s_1, s_2)$, and $X_2 = X_2(s_1, s_2)$.

The first energy functional comes from the theory of linear elasticity [2]:

$$E = \frac{1}{2}\sum_{i,j=1}^{3}\int_{\Omega_0} \lambda_E e_{ii} e_{jj} + 2\mu_E e_{ij} e_{ij} d\mathbf{s} \tag{87}$$

$$e_{ij} = \frac{1}{2}\left(\frac{\partial X_i}{\partial s_j} + \frac{\partial X_j}{\partial s_i}\right) - \delta_{ij} \tag{88}$$

where δ_{ij} is the Kronecker delta. The two-dimensional linear elastic energy functional is given by Eq. (87) with $X_3 = s_3$ and assuming $X_1 = X_1(s_1, s_2)$ and $X_2 = X_2(s_1, s_2)$. After simplifying, the equation for the two-dimensional linear elastic energy functional becomes

$$E = \frac{1}{2}\sum_{i,j=1}^{2}\int_{\Omega_0} \lambda_E e_{ii} e_{jj} + 2\mu_E e_{ij} e_{ij} d\mathbf{s} \tag{89}$$

The second is an isotropic neo-Hookean model [6] without any incompressibility-enforcing penalty term (see below):

$$E = \frac{1}{2}\int_{\Omega_0} \mu_E (I_1 - 3) d\mathbf{s} \tag{90}$$

where μ_E is the shear modulus and I_1 is the first invariant of the right Cauchy–Green deformation tensor as discussed in Section 2.1. In terms of the deformation map $\mathbf{x} = \mathbf{X}(\mathbf{s}, t)$, I_1 is given by

$$I_1 = \sum_{i,j=1}^{3} \frac{\partial X_i}{\partial s_j}\frac{\partial X_i}{\partial s_j} \tag{91}$$

We set $X_3 = s_3$ in this energy functional and assume $X_1 = X_1(s_1, s_2)$ and $X_2 = X_2(s_1, s_2)$ in order to derive the two-dimensional neo-Hookean model. Then the equation for the two-dimensional neo-Hookean model (after simplifying) is

$$E = \frac{1}{2}\int_{\Omega_0} \mu_E \left(\sum_{i,j=1}^{2} \frac{\partial X_i}{\partial s_j}\frac{\partial X_i}{\partial s_j} - 2\right) d\mathbf{s} \tag{92}$$

The derivation of the linear elasticity model assumes that the displacement is infinitesimal so we use it only for small displacements and use the neo-Hookean model for large displacements.

Eq. (90) is a simplified version of

$$E = \frac{1}{2}\int_{\Omega_0} \kappa_E (J-1)^2 + \mu_E\left(J^{-\frac{2}{3}} I_1 - 3\right) d\mathbf{s} \tag{93}$$

where J is the Jacobian of the deformation map $\mathbf{X}$. The first term in (93) is a penalty term that enforces incompressibility as $\kappa_E \to \infty$ [6]. Since the incompressibility condition is enforced through the velocity field in our formulation, we are free to set $J = 1$. This gives (90). In our tests using (93), which are not presented in this paper, the penalty term was the part of the discretization that restricted the timestep the most. Provided that the timestep was small enough for the computation involving (93) to be stable, results for these tests were very similar to the results when (90) was used. Also, we will show later that the method using (90) conserves area well when it is applied to the warm-up problem, and, therefore, the penalty term is unnecessary. The reason for this, of course, is that we enforce incompressibility via the divergence condition on the Eulerian velocity field.

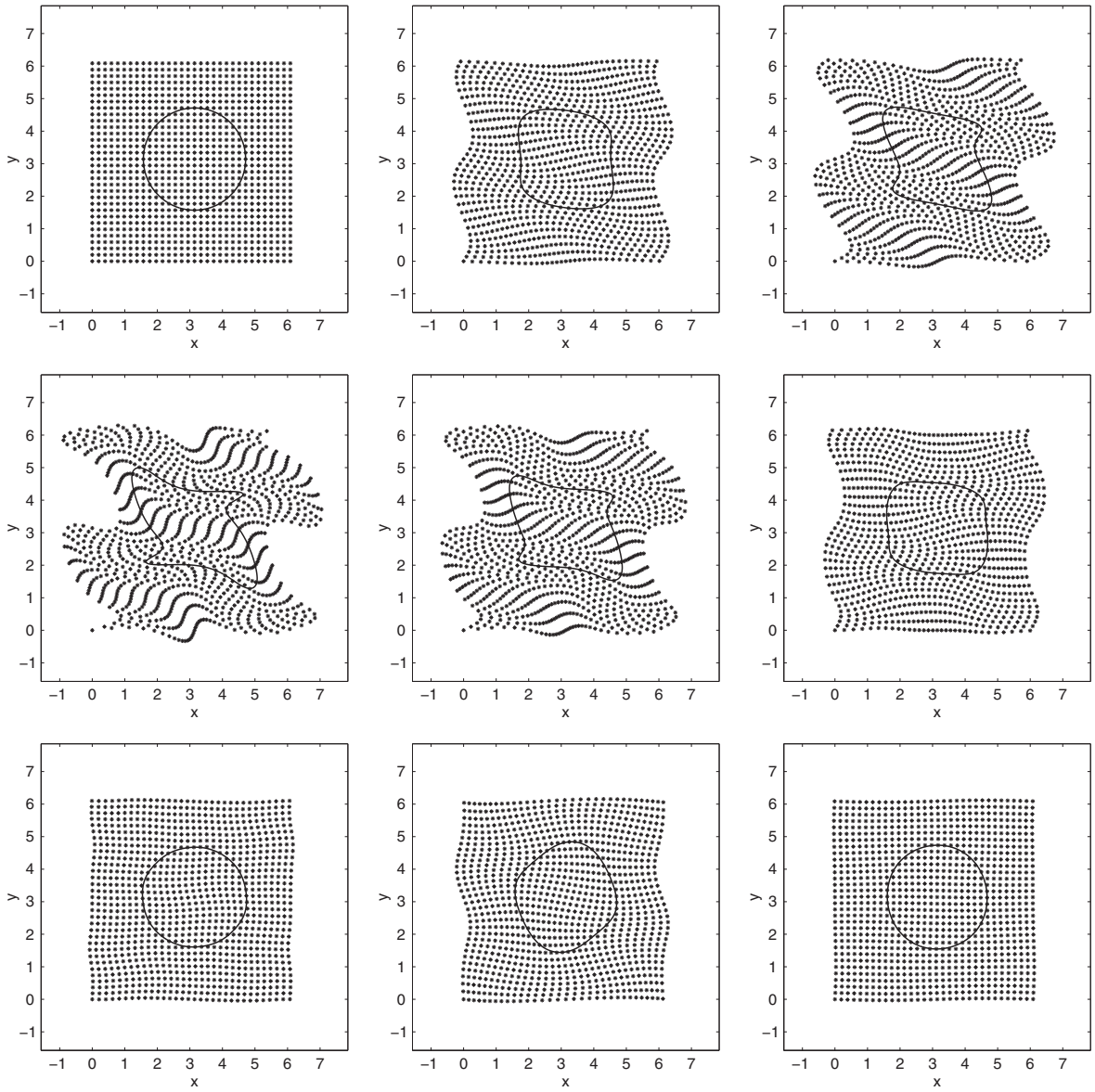

Fig. 1. Deformation of the elastic material at times $t = 0, 0.0712, 0.1816, 0.6111, 0.9793, 1.3474, 1.6665, 2.3047, 3.9270$. (Time increases from left to right in each row.) The energy functional is given by the neo-Hookean model. The 512×512 Eulerian grid that was used is much finer than the grid of Lagrangian markers used here to visualize the deformation. The solid curve has no mechanical significance. It moves with the material and is used for visualization and to check area conservation. Recall that our domain is square and periodic with period 2π. Each frame extends beyond this domain and we display only one period's worth of markers. The triangular mesh (not shown) was constructed by refining the coarse mesh described above 4 times. A timestep of $0.1h$ was used where h is the meshwidth for the Eulerian grid. The parameters were $\rho = 1.0$, $\mu = 0.5$, $\mu_E = 1.0$.

In the simulation using the linear elastic energy functional, the initial velocity $\mathbf{v}^0 = (v_1^0, v_2^0)$ was

$$v_1^0 = 0.5\sin(x+2y) + 0.125\sin(x-y) \tag{94}$$

$$v_2^0 = -0.25\sin(x+2y) + 0.125\sin(x-y) \tag{95}$$

The initial velocity for the simulation using the neo-Hookean model was 8 times larger, specifically:

$$v_1^0 = 4\sin(x+2y) + \sin(x-y) \tag{96}$$

$$v_2^0 = -2\sin(x+2y) + \sin(x-y) \tag{97}$$

In both simulations, we found as expected that the material deforms because of the initial velocity and undergoes damped oscillations around its reference configuration. The deformation in the simulation with the linear elastic energy functional is very small so we do not show the result as a figure here, although we shall report convergence results for this computation later. The deformation at various times for the simulation using the neo-Hookean model is shown in Fig. 1. Note that the points on the boundary satisfy periodic boundary conditions, but their motions are not constrained in any other way.

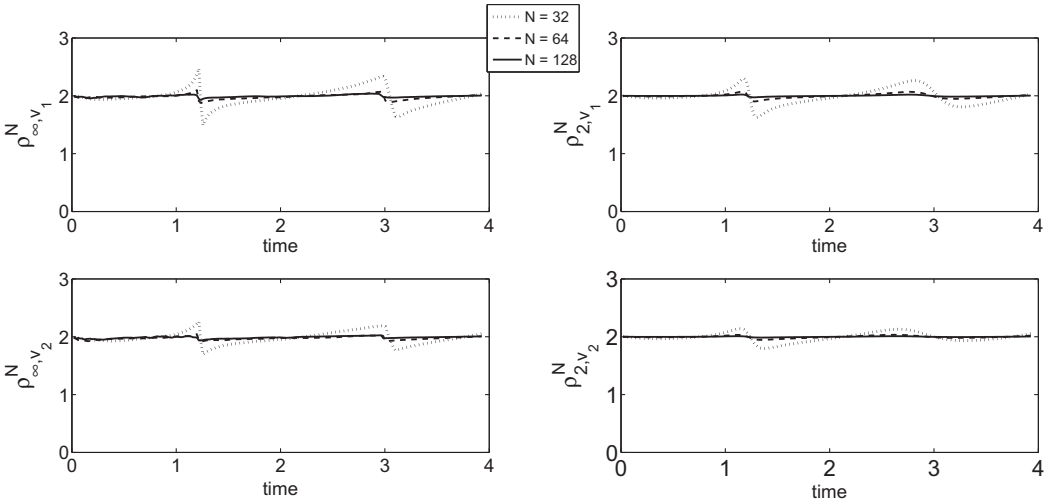

Fig. 2. Velocity field convergence rates as functions of time for the simulations in which the linear elasticity energy functional is used. The first column displays the L^∞ convergence rates and the second column displays the L^2 convergence rates. The plots of the convergence rates for v_1 are given in the first row and the plots of the convergence rates for v_2 are given in the second row. The solid curves represent the convergence rates on the finest set of grids; note that the values of these curves are very close to 2.

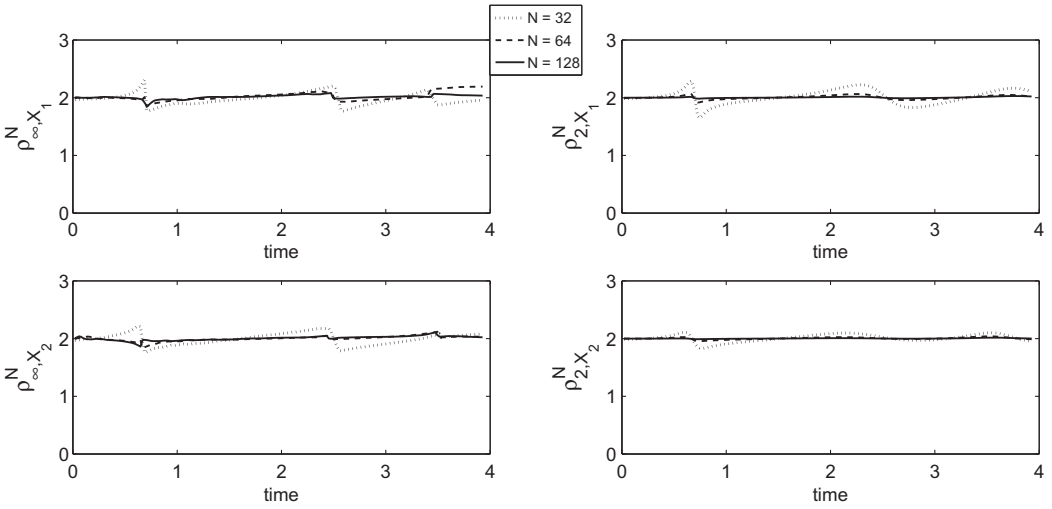

Fig. 3. Deformation map convergence rates as functions of time for the simulations in which the linear elasticity energy functional is used. The first column displays the L^∞ convergence rates and the second column displays the L^2 convergence rates. The plots of the convergence rates for X_1 are given in the first row and the plots of the convergence rates for X_2 are given in the second row. The solid curves represent the convergence rates on the finest set of grids; note that the values of these curves are very close to 2.

In addition to simulating the dynamics, we studied the convergence of the velocity field, the deformation map, and the elastic force density on the Eulerian grid by repeating the above simulations for different sizes of the Eulerian grid (and correspondingly the triangular mesh). We remark that studying the force density on the Eulerian grid was of interest because our application is one of the few applications of the immersed boundary method in which the Eulerian force density is a smooth function. In other applications, the singular nature of the delta function is not integrated out [8–10].

Let ϕ be a scalar-valued grid function defined on an uniform grid g^h of meshwidth h. We define the following two norms on the grid:

$$\|\phi\|_\infty = \max_{\mathbf{x}\in g^h} |\phi(\mathbf{x})| \tag{98}$$

$$\|\phi\|_2 = \left(\sum_{\mathbf{x}\in g^h} |\phi(\mathbf{x})|^2 h^2 \right)^{\frac{1}{2}} \tag{99}$$

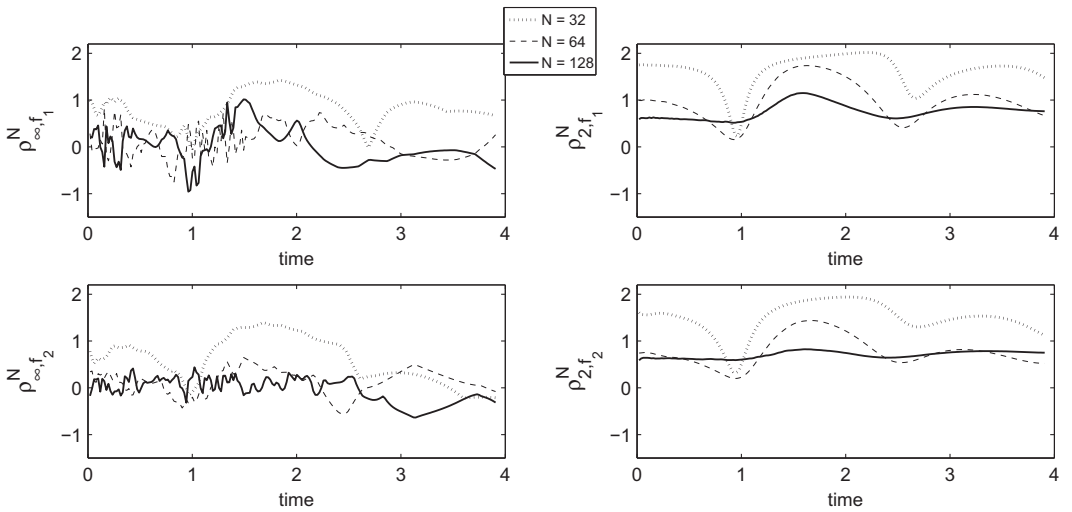

Fig. 4. Eulerian force density convergence rates as functions of time for the simulations in which the linear elasticity energy functional is used. The first column displays the L^∞ convergence rates and the second column displays the L^2 convergence rates. The plots of the convergence rates for f_1 are given in the first row and the plots of the convergence rates for f_2 are given in the second row. The solid curves represent the convergence rates on the finest set of grids. Note the different scale from that of the other convergence plots.

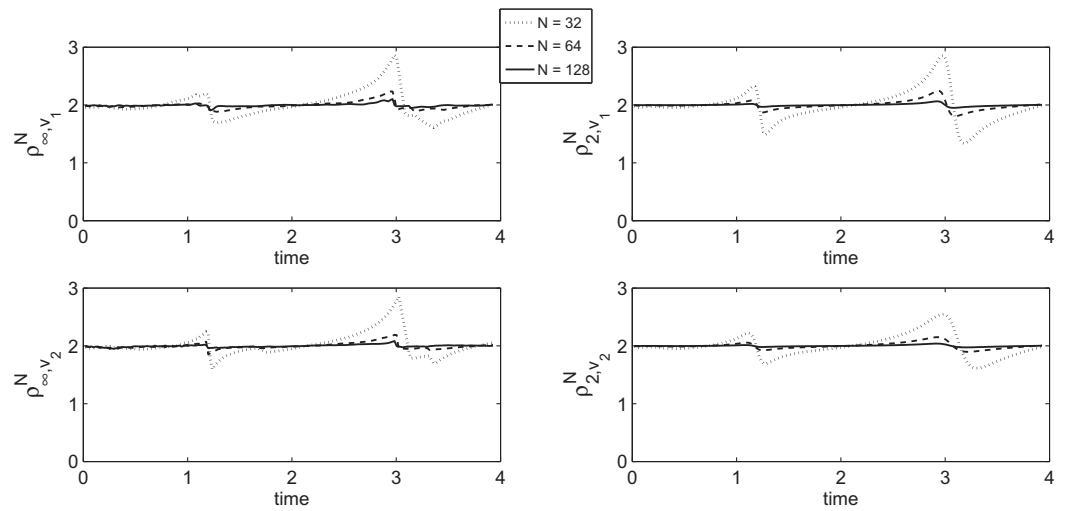

Fig. 5. Velocity field convergence rates as functions of time for the simulations in which the neo-Hookean model is used. The first column displays the L^∞ convergence rates and the second column displays the L^2 convergence rates. The plots of the convergence rates for v_1 are given in the first row and the plots of the convergence rates for v_2 are given in the second row. The solid curves represent the convergence rates on the finest set of grids; note that the values of these curves are very close to 2.

Let $\mathbf{v}^N(t)$ denote the approximation to velocity field at time t computed on an $N \times N$ Eulerian grid, and let $I^{2N\to N}\mathbf{v}^{2N}(t)$ be the restriction of $\mathbf{v}^{2N}(t)$ to the $N \times N$ Eulerian grid. The L^∞ norm of the change in each component of the velocity field when the computed solution on an $N \times N$ grid is compared to the computed solution on a $2N \times 2N$ grid is defined as

$$e^N_{\infty,v_i}(t) = \|v_i^N(t) - I^{2N\to N} v_i^{2N}(t)\|_\infty \tag{100}$$

Similarly, the L^2 norm of the difference is defined as

$$e^N_{2,v_i}(t) = \|v_i^N(t) - I^{2N\to N} v_i^{2N}(t)\|_2 \tag{101}$$

We define the convergence rates $\rho^N_{\infty,v_i}(t)$ and $\rho^N_{2,v_i}(t)$ by

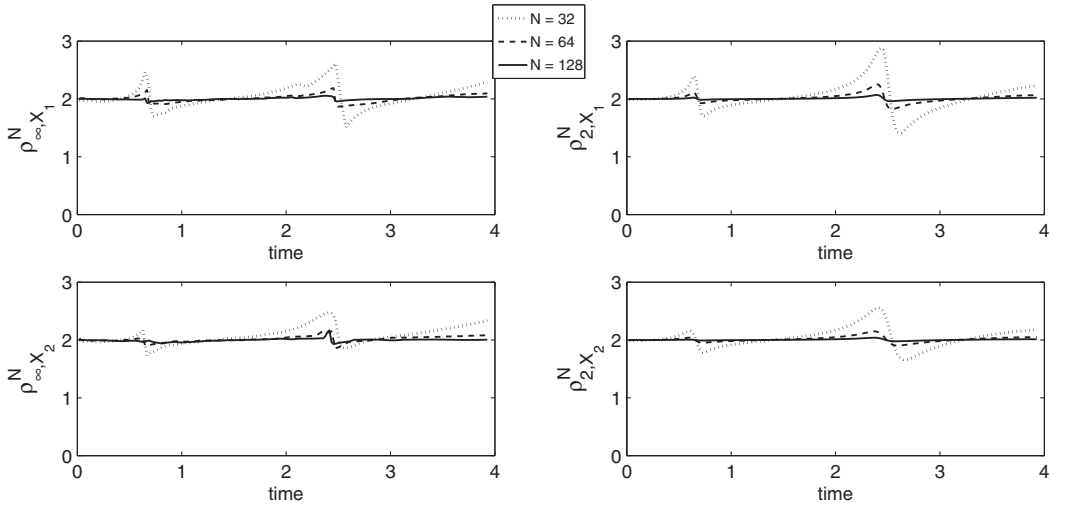

Fig. 6. Deformation map convergence rates as functions of time for the simulations in which the neo-Hookean model is used. The first column displays the L^∞ convergence rates and the second column displays the L^2 convergence rates. The plots of the convergence rates for X_1 are given in the first row and the plots of the convergence rates for X_2 are given in the second row. The solid curves represent the convergence rates on the finest set of grids; note that the values of these curves are very close to 2.

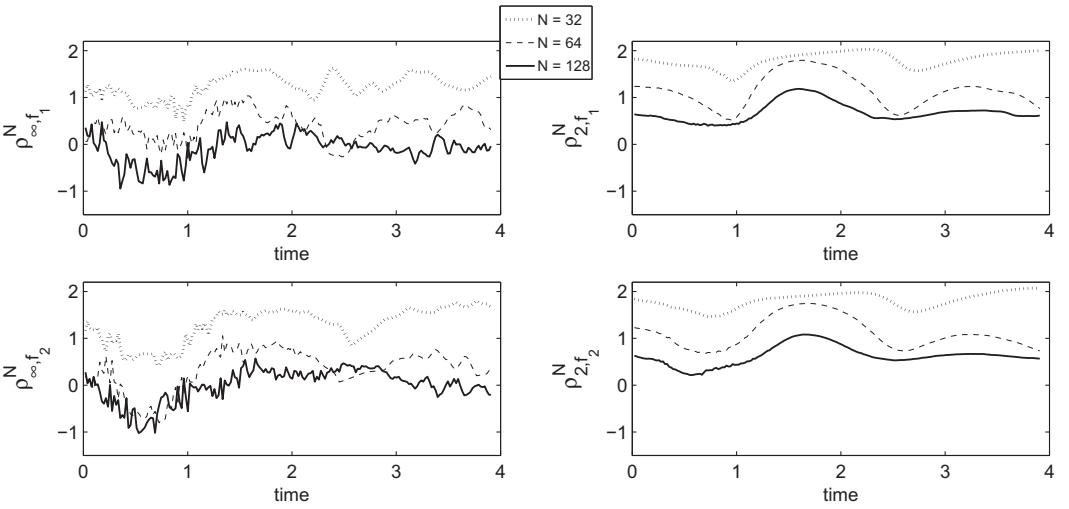

Fig. 7. Eulerian force density convergence rates as functions of time for the simulations in which the neo-Hookean model is used. The first column displays the L^∞ convergence rates and the second column displays the L^2 convergence rates. The plots of the convergence rates for f_1 are given in the first row and the plots of the convergence rates for f_2 are given in the second row. The solid curves represent the convergence rates on the finest set of grids. Note the different scale from that of the other convergence plots.

$$\rho^N_{\infty,v_i}(t) = \log_2\left(\frac{e^N_{\infty,v_i}(t)}{e^{2N}_{\infty,v_i}(t)}\right) \tag{102}$$

$$\rho^N_{2,v_i}(t) = \log_2\left(\frac{e^N_{2,v_i}(t)}{e^{2N}_{2,v_i}(t)}\right) \tag{103}$$

The convergence rates for the Eulerian force density are defined in a similar manner. Since the Eulerian force density is computed at the half timestep, the force density on successive grids do not correspond in time. To overcome this difficulty, we average the Eulerian force density at the $n+\frac{1}{2}$ timestep and $n+\frac{3}{2}$ timestep to obtain an approximation to the Eulerian force density at timestep $n+1$.

Since the deformation map is defined on the triangular mesh rather than the Eulerian grid, we must define norms on the triangular mesh. Let ϕ be a scalar-valued function defined on a triangular mesh and let $\phi^{(k)}$ denote its value at the kth node. Then we define the L^∞ norm as follows:

$$\|\phi\|_\infty = \max_{k=1,\ldots,N_v} |\phi^{(k)}| \tag{104}$$

The L^2 norm is defined similarly:

$$\|\phi\|_2 = \left(\sum_{k=1}^{N_v} |\phi^{(k)}|^2 h_e^2\right)^{\frac{1}{2}} \tag{105}$$

where $h_e = \frac{h}{2}$ is the average (or effective) meshwidth of our triangulation.

Let $\mathbf{X}^N(t)$ denote the approximation to the deformation map at time t calculated on the triangular mesh that corresponds to the $N \times N$ Eulerian grid; in particular, this triangular mesh is constructed by refining the coarse mesh described above $\log_2(N/32)$ times. Let $I^{2N\to N}\mathbf{X}^{2N}(t)$ be the restriction of $\mathbf{X}^{2N}(t)$ to this triangular mesh. Notice that $I^{2N\to N}\mathbf{X}^{2N}(t)$ is well-defined since our refinement procedure for the triangular mesh keeps the vertices from the old mesh. Then the L^∞ norm of the change for the ith component of the deformation map as the mesh is refined is

$$e^N_{\infty,X_i}(t) = \|X^N_i(t) - I^{2N\to N}X^{2N}_i(t)\|_\infty \tag{106}$$

The convergence rate $\rho^N_{\infty,X_i}(t)$ is defined as

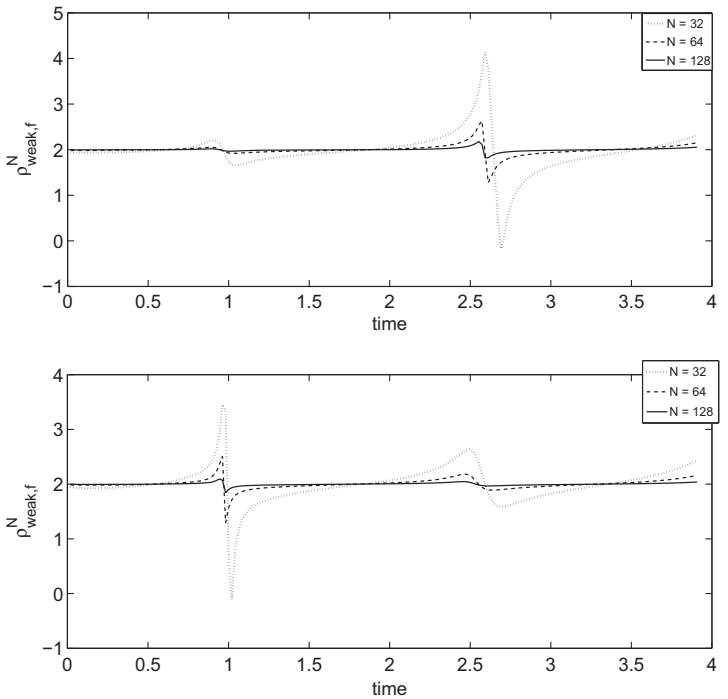

Fig. 8. Results of the weak convergence study for the Eulerian force density. The first graph is the plot of the convergence rates as functions of time for the simulations in which the linear elasticity functional is used. The second is the plot of the convergence rates for the simulations in which the neo-Hookean model is used. The solid curves represent the convergence rates on the finest set of grids; note that the values of these curves are very close to 2.

$$\rho^N_{\infty,X_i}(t) = \log_2\left(\frac{e^N_{\infty,X_i}(t)}{e^{2N}_{\infty,X_i}(t)}\right) \tag{107}$$

The corresponding quantities in the L^2 norm are defined similarly.

Figs. 2–7 give the plots of the convergence rates as functions of time. In the convergence study, the triangular mesh was refined with the Eulerian grid as described above. From these graphs, it seems clear that the velocity field and deformation map converge at second order. This is not true for the Eulerian force density. Notice that there are times when the L^∞ convergence rates for the Eulerian force density are negative; this means the error is increasing from one set of consecutive grids to the next.

Motivated by the immersed boundary formulation of the Eulerian force density and the nature of the delta function, we studied the weak convergence of the Eulerian force density. Given a smooth periodic test function $\mathbf{w} = (w_1, w_2)$, we performed a convergence study on the quantity

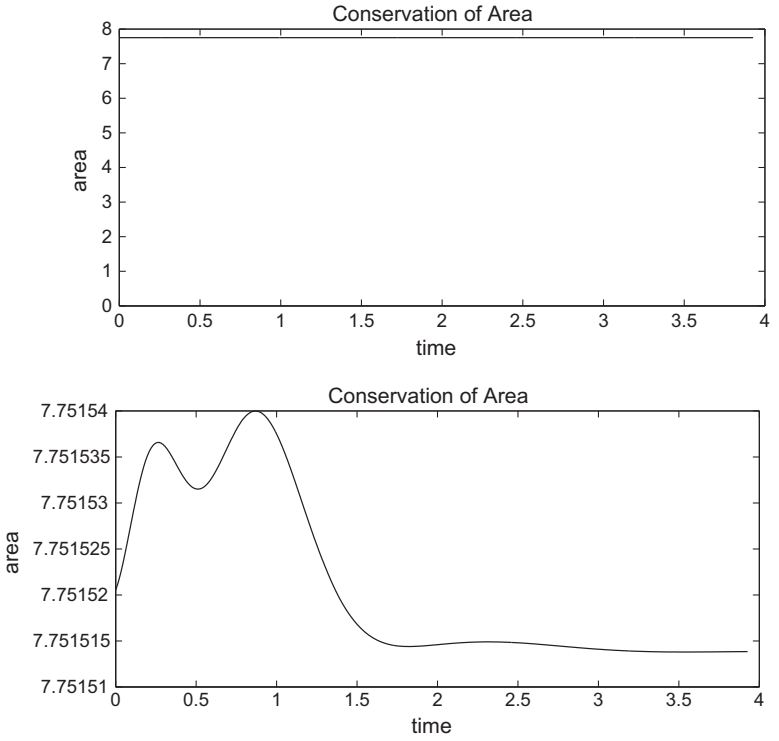

Fig. 9. Area of the disk as it deforms over time. The second graph is a rescaled version of the first graph to visualize the *small* errors in area conservation. Notice the scale of the second graph.

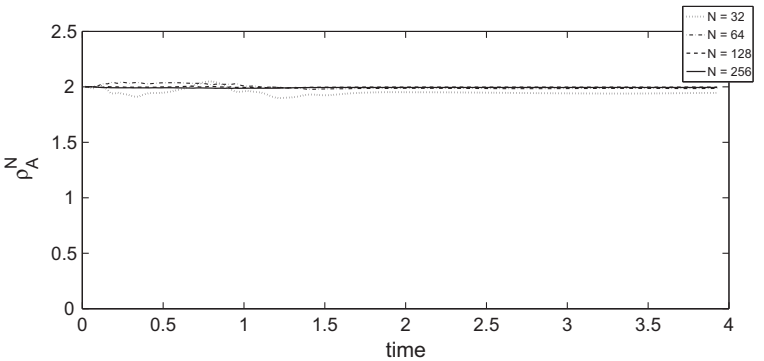

Fig. 10. Convergence rates from the area conservation study plotted as functions of time. With each refinement of the Eulerian grid, the finite element grid was refined and the number of Lagrangian points on the boundary of the disk was doubled. The solid curve is the plot of the convergence rate on the finest set of grids. Note how close the values of this curve are to 2.

$$P^N(t) = \sum_{\alpha=1}^{2} \sum_{\mathbf{x}\in g_\alpha^h} f_\alpha^N(\mathbf{x},t) w_\alpha(\mathbf{x}) h^2 \tag{108}$$

The change $e_P^N(t)$ and convergence rate $\rho_{\text{weak},f}^N(t)$ were given by

$$e_P^N(t) = |P^N(t) - P^{2N}(t)| \tag{109}$$

$$\rho_{\text{weak},f}^N(t) = \log_2\left(\frac{e_P^N(t)}{e_P^{2N}(t)}\right) \tag{110}$$

For the weak convergence study, we chose the test function with components:

$$\begin{aligned} w_1(x,y) = {} & 1 + 0.1\sin(x) + 0.2\sin(y) + 0.1\sin(2x) + 0.3\sin(x+y) + 0.2\sin(2y) + 0.4\sin(3x) + 0.1\sin(2x+y) \\ & + 0.2\sin(x+2y) + 0.3\sin(3y) \end{aligned} \tag{111}$$

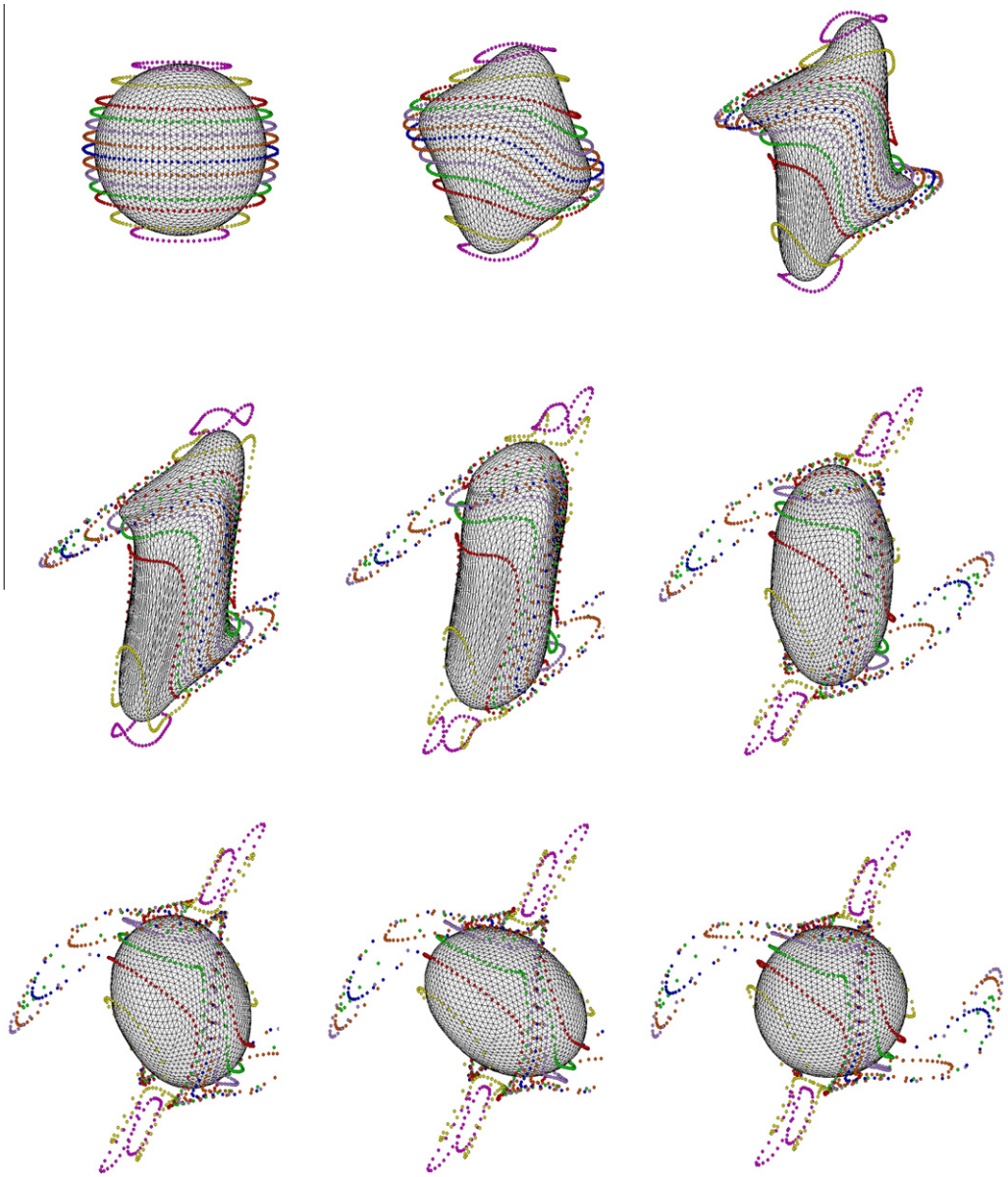

Fig. 11. Deformation of the elastic shell under the neo-Hookean material model at times t = 0, 0.157, 0.432, 0.982, 1.61, 2.63, 3.38, 4.16, 7.85. Time increases from left to right in each row. Fluid markers are used to visualize the deformation of the fluid near the elastic shell.

$$w_2(x,y) = 0.1 + 0.1\sin(x) + 0.1\sin(y) + 0.1\sin(2x) + 0.2\sin(x+y) + 0.1\sin(2y) + 0.1\sin(3x) + 0.2\sin(2x+y) + 0.3\sin(x+2y) + 0.4\sin(3y) \tag{112}$$

Fig. 8 gives the results of this convergence study for both choices of the energy functional. It seems clear from these plots that $P^N(t)$ converges at second order, at least for our particular choice of $\mathbf{w}$. This suggests that the Eulerian force density converges weakly at second order.

Finally, we studied how well the method using the neo-Hookean model (90) conserves area by calculating the change in area of a material disk under the deformation shown in Fig. 1. We chose the disk given by the equation

$$(x-\pi)^2 + (y-\pi)^2 \leqslant \frac{\pi}{2} \tag{113}$$

at time zero. In order to track the disk as it deforms, equally spaced Lagrangian points were placed on the boundary of the disk and these points were updated at each timestep through the same algorithm that was used to update the vertices of the triangles. Unlike the vertices of the triangles, however, the configuration of these Lagrangian points did not contribute to the

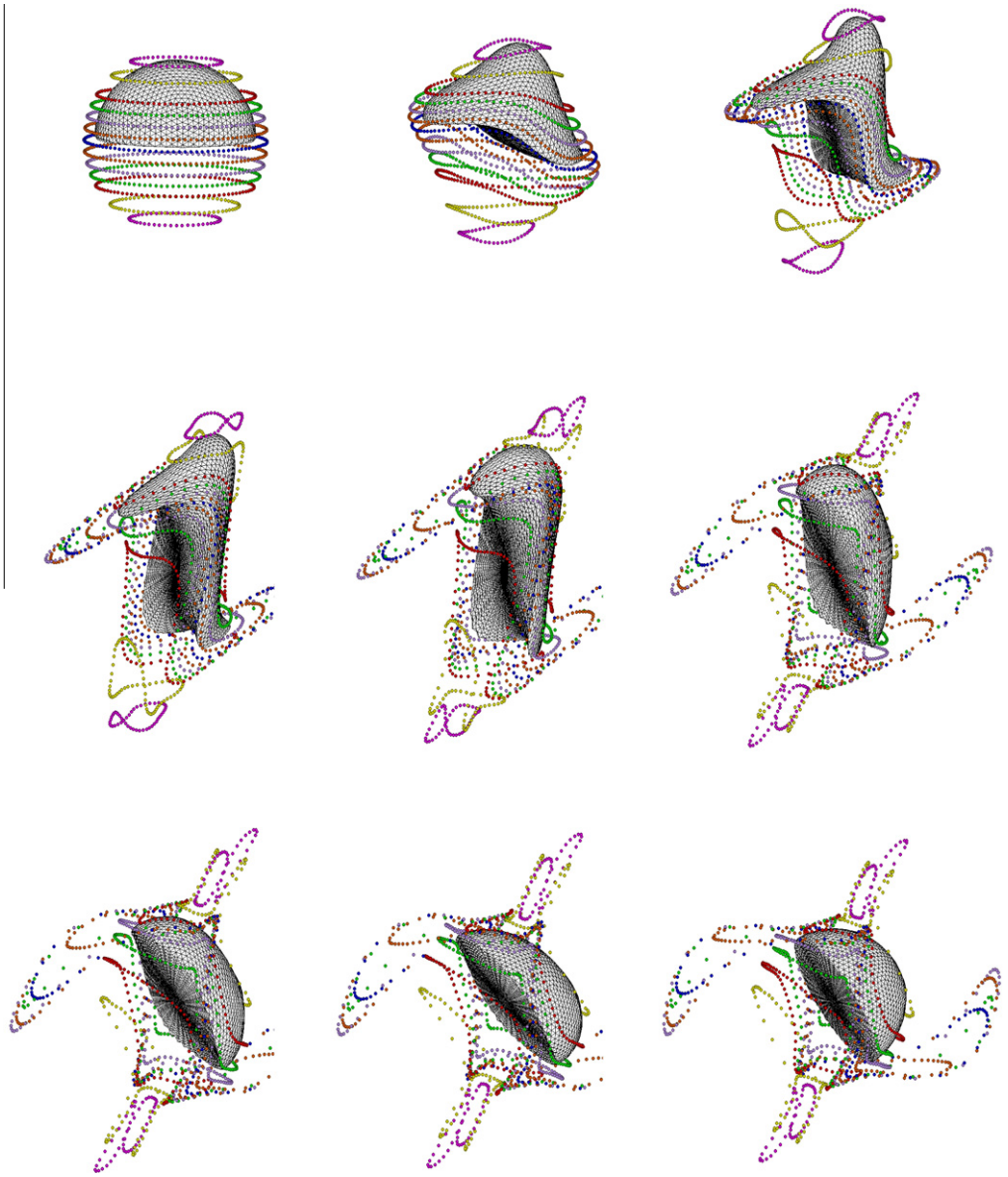

Fig. 12. Deformation of half of the elastic shell under the neo-Hookean material model at times $t = 0, 0.157, 0.432, 0.982, 1.61, 2.63, 3.38, 4.16, 7.85$. Time increases from left to right in each row. Fluid markers are used to visualize the deformation of the fluid near the elastic shell.

elastic forces of the system. We approximated the area of the deformed disk by the area of the polygon with these Lagrangian points as vertices.

Fig. 1 shows the current deformation of the disk for various times and Fig. 9 shows the area of the disk as a function of time. The largest change in area is 1.9466×10^{-5}, which should be compared to the initial area of $\pi^3/4 \approx 7.7516$. This suggests that incompressibility is well maintained by the method.

We also performed a convergence study on the area of the disk. Since the continuous velocity field is incompressible, the exact area of the disk at any time in the continuous problem is known and is equal to its initial area. Let $A^N(t)$ be the approximation to the area of the deformed disk at time t calculated from the simulation on the $N \times N$ Eulerian grid. Let A^0 be the initial area of the disk. We define the error as

$$e_A^N(t) = |A^N(t) - A^0| \tag{114}$$

and the convergence rate $\rho_A^N(t)$ as

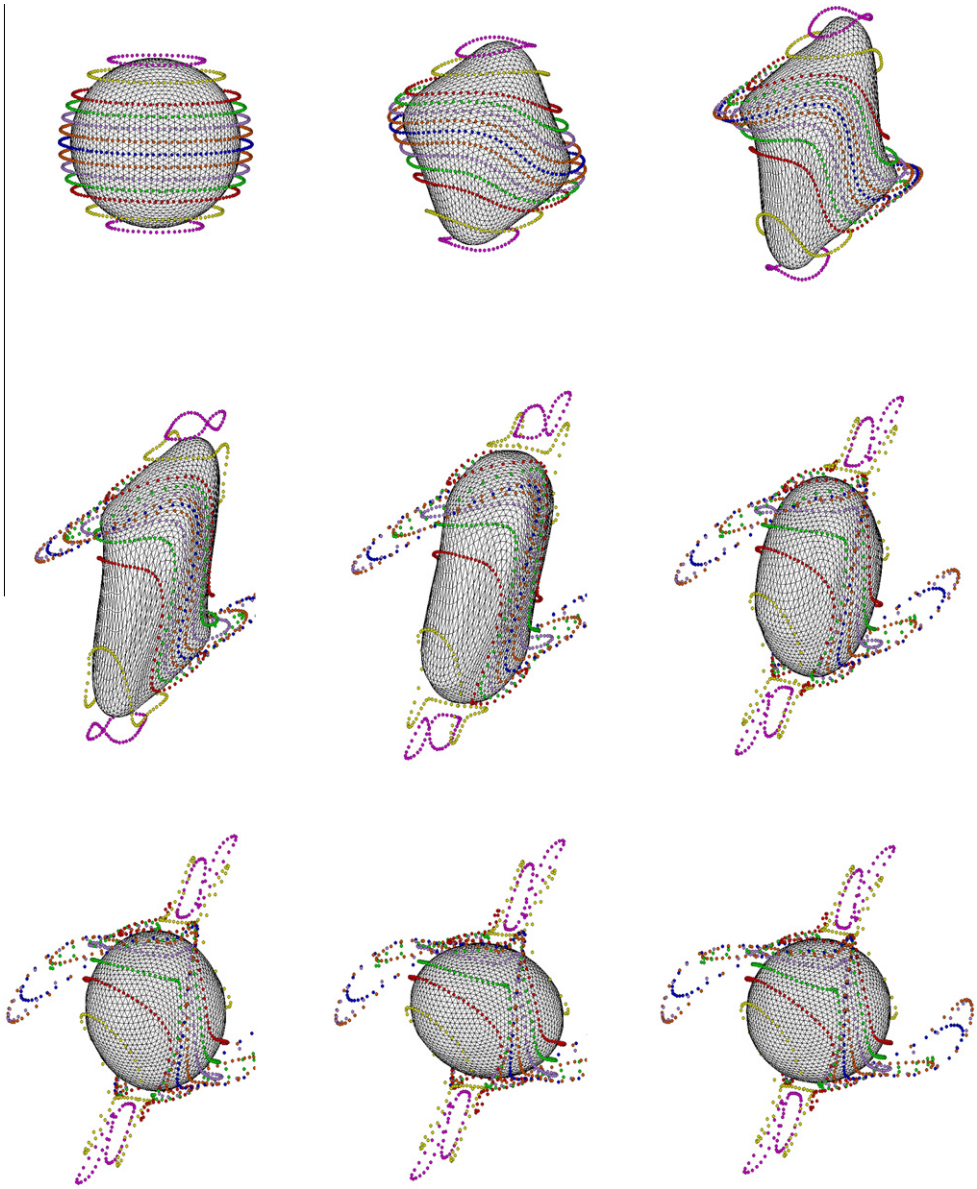

Fig. 13. Deformation of the elastic shell under the fiber-reinforced material model at times $t = 0$, 0.157, 0.432, 0.982, 1.61, 2.63, 3.38, 4.16, 7.85. Time increases from left to right in each row. Fluid markers are used to visualize the deformation of the fluid near the elastic shell.

$$\rho_A^N(t) = \log_2\left(\frac{e_A^N(t)}{e_A^{2N}(t)}\right) \tag{115}$$

Fig. 10 gives the results of this study. These results indicate that the area of the disk also converges at second order.

4.2. 3D results

In this section, we present our results for a three-dimensional fluid–structure interaction problem. An incompressible viscoelastic thick shell is immersed in an incompressible viscous fluid. The system is given an initial velocity which deforms the elastic shell and generates elastic forces. The viscoelastic shell undergoes large-amplitude damped oscillations around its reference configuration.

This problem is simulated under two choices of the elastic energy functional. The first is a three-dimensional isotropic neo-Hookean model without any incompressibility-enforcing term [6]:

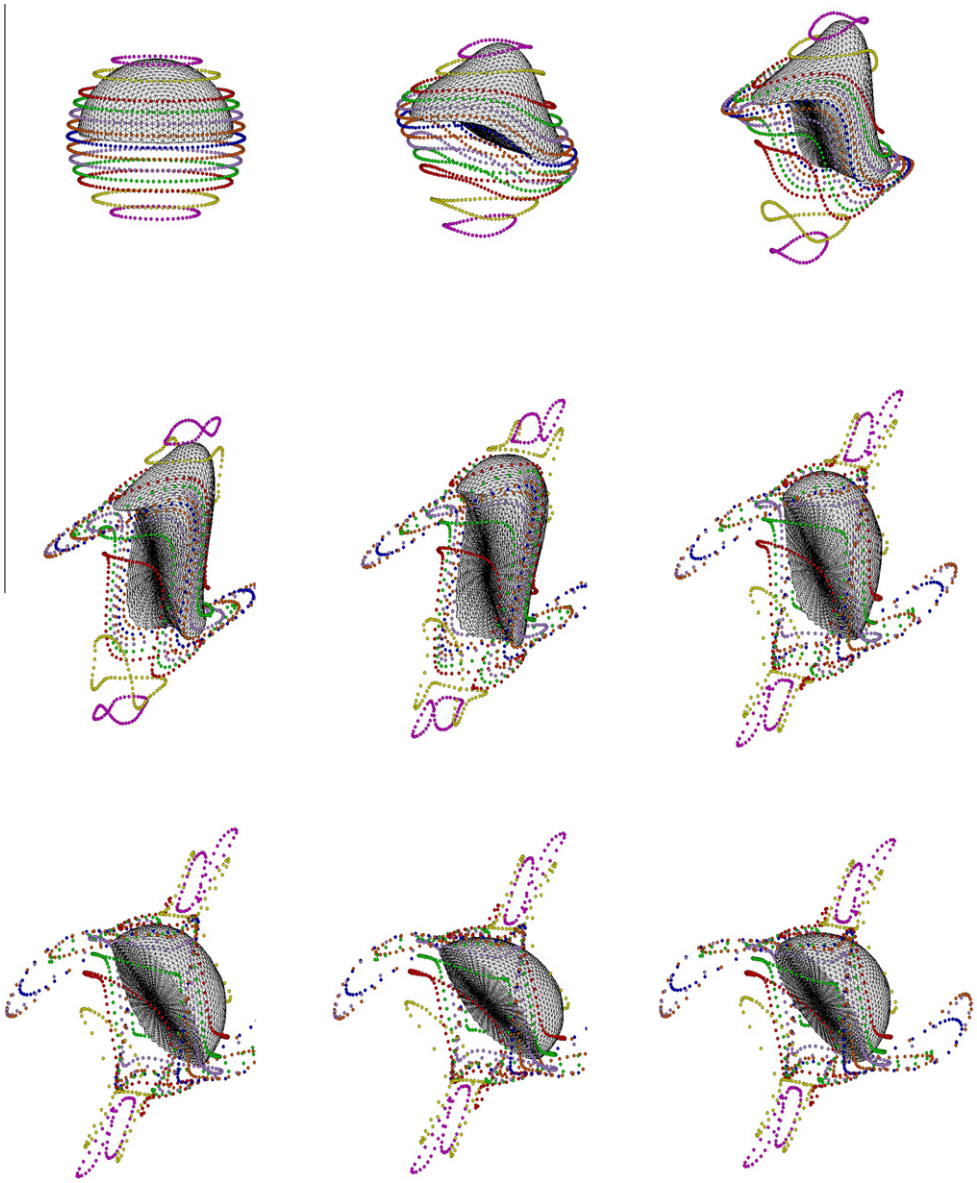

Fig. 14. Deformation of half of the elastic shell under the fiber-reinforced material model at times $t = 0, 0.157, 0.432, 0.982, 1.61, 2.63, 3.38, 4.16, 7.85$. Time increases from left to right in each row. Fluid markers are used to visualize the deformation of the fluid near the elastic shell.

$$E = \frac{1}{2}\int_{\Omega_0} \mu_E(I_1 - 3)d\mathbf{s} \tag{116}$$

The second is the standard fiber-reinforced model [7], also without any incompressibility-enforcing term. It models a composite material in which fibers (all running in the same direction **a** in the reference configuration) are embedded into a background isotropic neo-Hookean material. The equation for the energy functional is

$$E = \frac{1}{2}\int_{\Omega_0} \mu_E(I_1 - 3 + \gamma(I_4 - 1)^2)d\mathbf{s} \tag{117}$$

where

$$I_4 = \mathbf{a}^T\mathbb{F}^T\mathbb{F}\mathbf{a} \tag{118}$$

is the stretch in the fibers and μ_E is the shear modulus. The parameter γ is dimensionless and determines the relative strength of the fiber reinforcement. Note that **a** is a constant vector in this model. We take the fiber direction to be the z-axis for convenience and think of the thick elastic shell as being cut out of a block of this composite material.

In the immersed boundary method described in this paper, the Lagrangian mesh is independent of the material model. In particular, we use the same tetrahedral mesh for the elastic shell in the simulations for the two elastic energy functionals described above. To change the material model within our immersed boundary method, only $\partial W/\partial a_{ij}$ in the formula for $\mathbf{F}_T^{(k)}$ (Eq. (51)) must be altered.

Since the elastic shell does not take up the entire spatial domain, $\Omega_0 \subsetneq \Omega$, there are interfaces at which the elastic material and the fluid meet. In the continuous formulation of the problem, there are boundary terms that arise at these interfaces when integration by parts is done in calculating the Lagrangian force density from the elastic energy functional. As shown by Heltai [11], these boundary terms take the form of a delta-function layer of force that is concentrated on the solid–fluid interface, in addition to the finite Lagrangian force density that appears in the interior of the elastic material.

In our energy-based formulation, however, this happens automatically in the following way. Recall that the Lagrangian force at each node is a sum of contributions from each of the tetrahedra which touch that node. At interior nodes, these forces nearly cancel, leaving a small resulting force which is $O(h^3)$ per node, thus generating a finite force per unit volume. At interfacial nodes, there is less cancellation, and the resultant force is $O(h^2)$ per node, thus generating a finite amount of force per unit area of interface. We emphasize, however, that from an algorithmic point of view, all of the nodes are treated in exactly the same way in our method, with no distinction being made between interfacial and interior nodes. This is true both with regard to the Lagrangian force computation, and also with regard to the spreading of force from the Lagrangian nodes to the Eulerian mesh.

As described in Section 3, we use a staggered grid to discretize the fluid domain and a tetrahedral mesh to discretize the elastic shell. The construction of the tetrahedral mesh used in the simulation is described in Appendix D. The spatial domain for the computation was $[0, 2\pi]^3$ which was discretized using a $128 \times 128 \times 128$ Eulerian grid. At time zero, the coordinates of the center of the elastic shell were (π, π, π), and the elastic shell had an outer radius of 1.5 and an inner radius of approximately 0.2382.

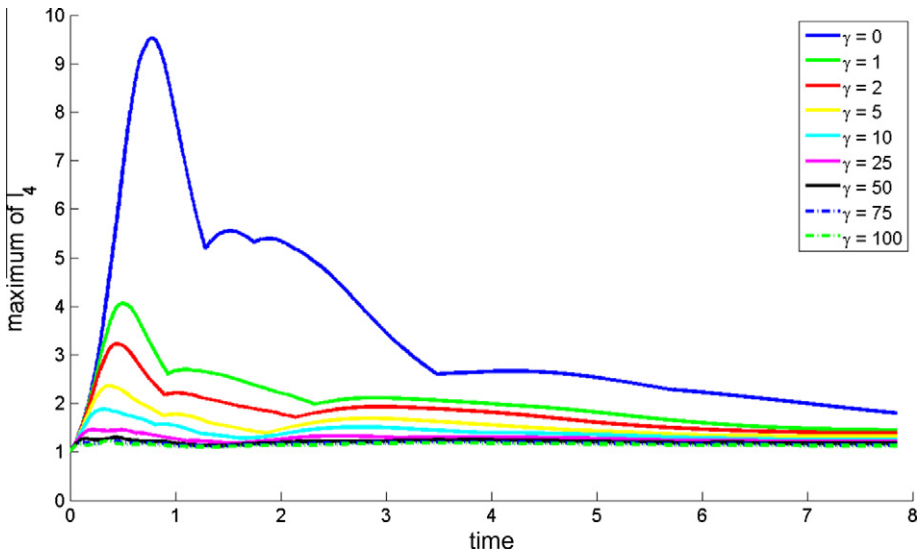

Fig. 15. Local stretch in the fibers for several values of γ (the relative strength of the fiber reinforcement). The maximum of I_4 was taken over the elements and used as the measure of local stretch. The kinks in the curves are the cross-overs of the stretch curves for different elements.

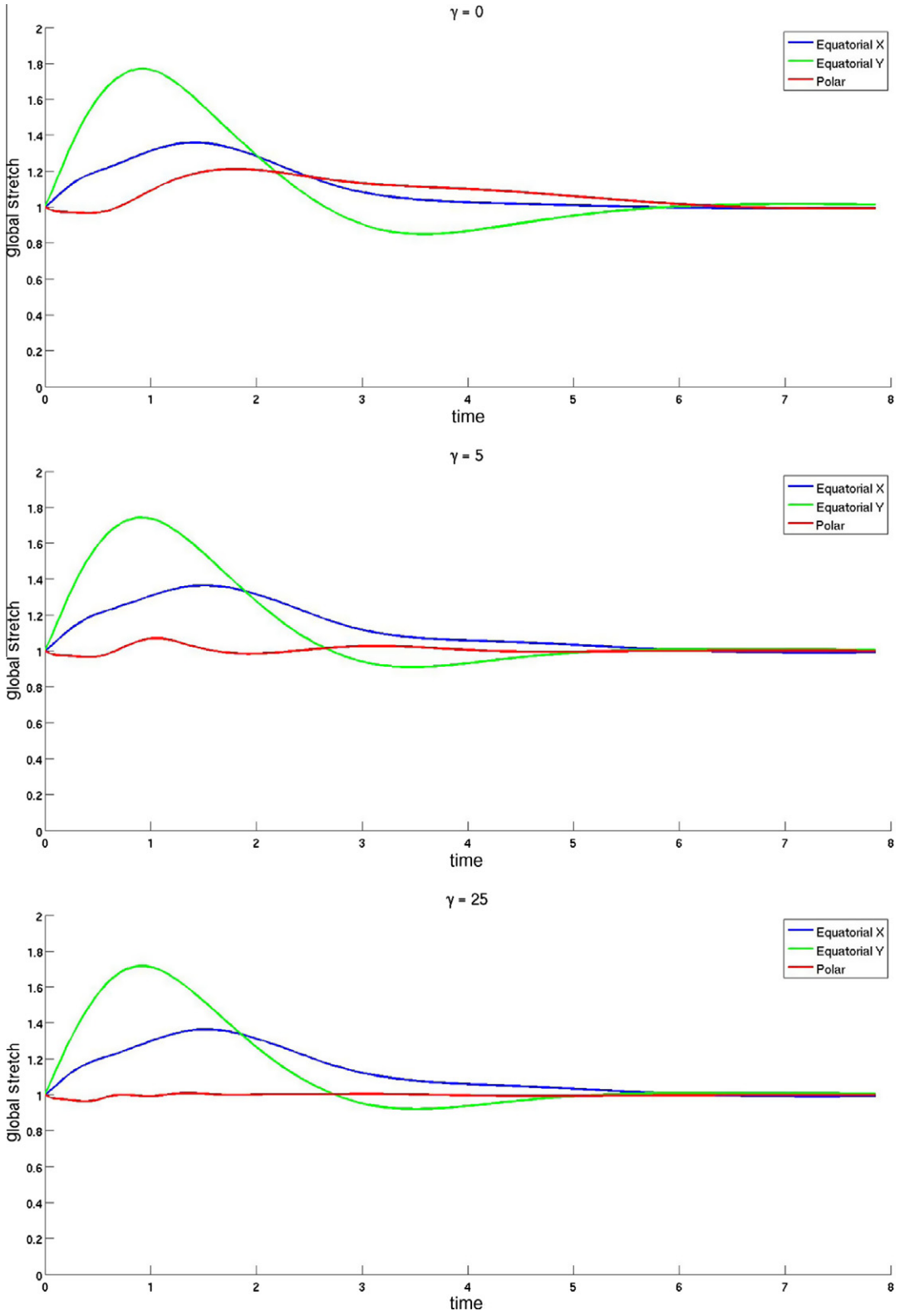

Fig. 16. Global stretch in the fibers. We used the normalized distance between material points on the elastic shell to measure global stretch. The global stretch was calculated for three pairs of points: the north and south poles on the outer surface of the elastic shell (denoted by 'Polar' in the plots); the two points on the equator of the outer surface that intersect the *x*-axis (denoted by 'Equatorial X' in the plots); and the two points on the equator of the outer surface that intersect the *y*-axis (denoted by 'Equatorial Y' in the plots). The global stretch for three pairs of points as functions of time is shown in each plot for a fixed value of γ.

The initial velocity $\mathbf{v}^0 = (v_1^0, v_2^0, v_3^0)$ for all simulations were

$$v_1^0 = 1.4\sin(x+2y+z) + 0.8\sin(x-y+z) \tag{119}$$

$$v_2^0 = -\sin(x+2y+z) + 2\sin(x-y+z) \tag{120}$$

$$v_3^0 = 0.6\sin(x+2y+z) + 1.2\sin(x-y+z) \tag{121}$$

We chose the timestep to be $0.1h$ to satisfy the CFL condition for the advection term in the fluid equations where h is the meshwidth for the Eulerian grid. The physical parameters were

$$\rho = 1.0, \quad \mu = 0.25, \quad \mu_E = 1.0 \tag{122}$$

where ρ is the density of the material, μ is the viscosity, and μ_E is the shear modulus (see Eqs. (116) and (117)).

Figs. 11 and 12 show the deformation of the shell at various times under the isotropic neo-Hookean model (Eq. (116)). Figs. 13 and 14 show the deformation of the shell at various times under the fiber-reinforced material model with $\gamma = 25$ (Eq. (117)). Figs. 12 and 14 show only half of the shell so the deformation of the inside of the shell in each of the simulations can be visualized. Fluid markers have been included so that the deformation of the fluid can be appreciated.

Although the material is stiffer in the second simulation because of the fiber reinforcement, the two simulations produce very similar dynamics, and it is difficult to perceive the differences in the two simulations from the stills in Figs. 11–14. To show that the fiber reinforcement stiffens the material in the fiber direction, we computed the stretch in the fibers locally and globally as the relative strength of the fiber reinforcement increases.

Recall that I_4 is the fiber stretch, and it is given by the formula

$$I_4 = \mathbf{a}^T \mathbb{F}^T \mathbb{F} \mathbf{a} \tag{123}$$

Since each element deforms linearly, the deformation gradient $\mathbb{F}$ is constant on each element, and, therefore, I_4 is constant on each element. We took the maximum of I_4 over the elements in the finite element mesh as our measure of stretch in the fibers locally.

To study the stretch in the fibers on a global scale, we computed the distance between material points on the elastic shell normalized by their initial distance. We looked at the global stretch for the following three pairs of points: the north and south poles on the outer surface of the elastic shell; the two points on the equator of the outer surface that intersect the x-axis; and the two points on the equator of the outer surface that intersect the y-axis.

The local stretch in the fibers as a function of time is plotted in Fig. 15 for several values of γ. It is clear from this figure that increasing the relative strength of the fiber reinforcement decreases the stretch in the fibers locally. For large values of gamma there is almost no local stretch in the fibers. We remark that the kinks in the curves are a consequence of taking the maximum norm. In other words, the stretch curves corresponding to different elements cross each other at the locations of the kinks.

The global stretch for the three pairs of points are plotted in Fig. 16 as functions of time for three values of gamma. Note that increasing the relative strength of the fiber reinforcement affects only the pair of points on the polar axis. This is to be expected since fibers run in the polar direction. It is then clear from these plots that the fiber reinforcement stiffens the material in the fiber direction. Note also that the oscillations appear in the global stretch curve for the polar points as $\gamma \to \infty$. This indicates that the material is stiffening in the fiber direction. Despite this extra stiffness, we were able to use the same timestep (see above) for all of the simulations.

5. Conclusion

In this paper, we introduced a model for incompressible viscoelasticity in which Lagrangian coordinates are used to describe elastic forces and Eulerian coordinates are used for the equations of motion and incompressibility condition. No stress tensors are needed, since the elastic forces are computed directly from an energy functional. A discretization of the model was presented in which forces are computed on a Lagrangian tetrahedral mesh and the velocity field is computed via finite differences on a staggered grid. The immersed boundary method is the mechanism by which communication takes place between the Lagrangian mesh and Eulerian grid.

The method was first applied to a warm-up problem in two dimensions in which an incompressible viscoelastic material fills a periodic domain. The convergence rates of the velocity field, the deformation map, and the Eulerian force density were studied for this problem and the numerical results suggested that the velocity field and deformation map converge at second order. The results also indicated that the Eulerian force density converges weakly at second order.

We also studied how well the method conserves area for the two-dimensional problem. The results revealed that incompressibility is well maintained by the method. This implies that penalty terms, which are conventionally used to enforce volume conservation and which can cause severe timestep restrictions, can be omitted in the formulation of the energy model when our method is used in studying the dynamics of an incompressible viscoelastic material.

Finally, we demonstrated that the method can be applied to fluid–structure interaction problems by using the method to simulate the dynamics of a three-dimensional thick viscoelastic shell in an incompressible viscous fluid. This problem was simulated for two materials: an isotropic neo-Hookean model and an anisotropic fiber-reinforced model. The example demonstrates the ease with which one material model can be swapped for another material model.

In order to apply the present form of our method in the context of fluid–structure interaction, we have to assume that the density and viscosity of the elastic structure are matched to those of the surrounding fluid. Several immersed boundary methods for non-uniform density [13–15] already exist, however, and an immersed boundary method for non-uniform viscosity is under development, so these restrictions are not fundamental. It should therefore be straightforward to extend the present work to problems involving immersed incompressible elastic materials whose properties may differ from those of the ambient fluid. We will then have a very general tool for the study of fluid–structure interaction.

Acknowledgements

DD is funded by the Henry MacCracken Fellowship and has also received support from NSF grant DMS-0914827.

Appendix A

Recall,

$$E[\mathbf{X}] = \int_{\Omega_0} W(\mathbb{F}) d\mathbf{s} \tag{A.1}$$

and

$$\mathbb{P}_{ij} = \frac{\partial W}{\partial \mathbb{F}_{ij}} \tag{A.2}$$

First we calculate $\frac{\delta E}{\delta X}$ using the definition given in the paragraph following (10).
Let

$$\phi_{\delta \mathbf{X}}(\alpha) = E[\mathbf{X} + \alpha \delta \mathbf{X}] = \int_{\Omega_0} W\left(\frac{\partial \mathbf{X}}{\partial \mathbf{s}} + \alpha \frac{\partial \delta \mathbf{X}}{\partial \mathbf{s}}\right) d\mathbf{s} \tag{A.3}$$

Then

$$\left.\frac{d\phi_{\delta \mathbf{X}}}{d\alpha}\right|_{\alpha=0} = \sum_{i,j=1}^{3} \int_{\Omega_0} \frac{\partial W}{\partial \mathbb{F}_{ij}} \frac{\partial \delta X_i}{\partial s_j} d\mathbf{s} \tag{A.4}$$

$$= \sum_{i,j=1}^{3} \int_{\Omega_0} \mathbb{P}_{ij} \frac{\partial \delta X_i}{\partial s_j} d\mathbf{s} \tag{A.5}$$

$$= -\sum_{i,j=1}^{3} \int_{\Omega_0} \frac{\partial \mathbb{P}_{ij}}{\partial s_j} \delta X_i d\mathbf{s} \tag{A.6}$$

The chain rule was used in the first equality and (A.2) in the second equality. In the last equality, we used integration by parts and assumed that the boundary terms cancel out, which is the case when we use periodic boundary conditions for the velocity field.

By the definition of the variational derivative

$$\left(\frac{\delta E}{\delta \mathbf{X}}\right)_i = -\sum_{j=1}^{3} \frac{\partial \mathbb{P}_{ij}}{\partial s_j} \tag{A.7}$$

This is the componentwise expression of the equation

$$\frac{\delta E}{\delta \mathbf{X}} = -\nabla_{\mathbf{s}} \cdot \mathbb{P} \tag{A.8}$$

Appendix B

From (14), the Eulerian force density $\mathbf{f}(\mathbf{x}, t)$ corresponding to $\frac{\delta E}{\delta \mathbf{X}}$ is

$$\mathbf{f}(\mathbf{x}, t) = \frac{1}{J(\mathbf{X}^{-1}(\mathbf{x}, t), t)} \frac{\delta E}{\delta \mathbf{X}}(\mathbf{X}^{-1}(\mathbf{x}, t), t) \tag{B.1}$$

Similarly, the Eulerian force density $\hat{\mathbf{f}}(\mathbf{x}, t)$ corresponding to $\frac{\delta \widehat{E}}{\delta \mathbf{X}}$ (where $\widehat{E}$ is given by Eq. (26)) is

$$\hat{\mathbf{f}}(\mathbf{x}, t) = \frac{1}{J(\mathbf{X}^{-1}(\mathbf{x}, t), t)} \frac{\delta \widehat{E}}{\delta \mathbf{X}}(\mathbf{X}^{-1}(\mathbf{x}, t), t) \tag{B.2}$$

We will prove that

$$\mathbf{f}(\mathbf{x}, t) - \hat{\mathbf{f}}(\mathbf{x}, t) = \nabla_{\mathbf{x}} q(\mathbf{x}, t) \tag{B.3}$$

for some scalar-valued function q.

Recall that for an isotropic material

$$E[\mathbf{X}] = \int_{\Omega_0} W(I_1, I_2, I_3) d\mathbf{s} \tag{B.4}$$

Also,

$$\widehat{E}[\mathbf{X}] = \int_{\Omega_0} W(I_1, I_2, 1) d\mathbf{s} \tag{B.5}$$

To simplify the calculations, we shall write W as a function of J instead of I_3. This does not change $\widehat{E}[\mathbf{X}]$ since $J \equiv 1$ implies that $I_3 \equiv 1$ by the identity $I_3 = J^2$.

Given a perturbation $\delta\mathbf{X} = \delta\mathbf{X}(\mathbf{s})$, let

$$I_1^\alpha = I_1(\mathbf{X} + \alpha\delta\mathbf{X}) \tag{B.6}$$
$$I_2^\alpha = I_2(\mathbf{X} + \alpha\delta\mathbf{X}) \tag{B.7}$$
$$J^\alpha = J(\mathbf{X} + \alpha\delta\mathbf{X}) \tag{B.8}$$

As in the definition of the variational derivative given in the paragraph following (10), we define

$$\phi_{\delta\mathbf{X}}(\alpha) = E[\mathbf{X} + \alpha\delta\mathbf{X}] = \int_{\Omega_0} W(I_1^\alpha, I_2^\alpha, J^\alpha) d\mathbf{s} \tag{B.9}$$

and

$$\hat{\phi}_{\delta\mathbf{X}}(\alpha) = \widehat{E}[\mathbf{X} + \alpha\delta\mathbf{X}] = \int_{\Omega_0} W(I_1^\alpha, I_2^\alpha, 1) d\mathbf{s} \tag{B.10}$$

Using these definitions we have

$$\left.\frac{d\phi_{\delta\mathbf{X}}}{d\alpha}\right|_{\alpha=0} = \int_{\Omega_0} \left.\frac{\partial W}{\partial I_1}\frac{dI_1^\alpha}{d\alpha}\right|_{\alpha=0} + \left.\frac{\partial W}{\partial I_2}\frac{dI_2^\alpha}{d\alpha}\right|_{\alpha=0} + \left.\frac{\partial W}{\partial J}\frac{dJ^\alpha}{d\alpha}\right|_{\alpha=0} d\mathbf{s} \tag{B.11}$$

and

$$\left.\frac{d\hat{\phi}_{\delta\mathbf{X}}}{d\alpha}\right|_{\alpha=0} = \int_{\Omega_0} \left.\frac{\partial W}{\partial I_1}\frac{dI_1^\alpha}{d\alpha}\right|_{\alpha=0} + \left.\frac{\partial W}{\partial I_2}\frac{dI_2^\alpha}{d\alpha}\right|_{\alpha=0} d\mathbf{s} \tag{B.12}$$

Since

$$\int_{\Omega_0} \frac{\delta E}{\delta \mathbf{X}} \cdot \delta\mathbf{X} d\mathbf{s} = \left.\frac{d\phi_{\delta\mathbf{X}}}{d\alpha}\right|_{\alpha=0} \tag{B.13}$$
$$\int_{\Omega_0} \frac{\delta \widehat{E}}{\delta \mathbf{X}} \cdot \delta\mathbf{X} d\mathbf{s} = \left.\frac{d\hat{\phi}_{\delta\mathbf{X}}}{d\alpha}\right|_{\alpha=0} \tag{B.14}$$

we have

$$\int_{\Omega_0} \left(\frac{\delta E}{\delta \mathbf{X}} - \frac{\delta \widehat{E}}{\delta \mathbf{X}}\right) \cdot \delta\mathbf{X} d\mathbf{s} = \int_{\Omega_0} \left.\frac{\partial W}{\partial J}\frac{dJ^\alpha}{d\alpha}\right|_{\alpha=0} d\mathbf{s} \tag{B.15}$$

Using the definition of J^α, it can be shown that

$$\left.\frac{dJ^\alpha}{d\alpha}\right|_{\alpha=0} = \det\left(\frac{\partial \mathbf{X}}{\partial \mathbf{s}}\right) \mathrm{tr}\left(\left(\frac{\partial \mathbf{X}}{\partial \mathbf{s}}\right)^{-1} \frac{\partial \delta\mathbf{X}}{\partial \mathbf{s}}\right) \tag{B.16}$$
$$= J\mathrm{tr}\left(\mathbb{F}^{-1}\frac{\partial \delta\mathbf{X}}{\partial \mathbf{s}}\right) \tag{B.17}$$
$$= J\sum_{i,j=1}^{3} \mathbb{F}^{-1}_{ji}\frac{\partial \delta X_i}{\partial s_j} \tag{B.18}$$

Then

$$\int_{\Omega_0} \left(\frac{\delta E}{\delta \mathbf{X}} - \frac{\delta \widehat{E}}{\delta \mathbf{X}}\right) \cdot \delta\mathbf{X} d\mathbf{s} = \sum_{i,j=1}^{3} \int_{\Omega_0} \frac{\partial W}{\partial J} J\mathbb{F}^{-1}_{ji}\frac{\partial \delta X_i}{\partial s_j} d\mathbf{s} \tag{B.19}$$
$$= \sum_{i,j=1}^{3} \int_{\Omega} \left[\frac{\partial W}{\partial J}\mathbb{F}^{-1}_{ji}\frac{\partial \delta X_i}{\partial s_j}\right]\Big|_{\mathbf{s}=\mathbf{X}^{-1}(\mathbf{x},t)} d\mathbf{x} \tag{B.20}$$

where we used the change of variables $\mathbf{x} = \mathbf{X}(\mathbf{s},t)$ in the last equality.

The chain rule gives the following identity:

$$\frac{\partial}{\partial s_j} = \sum_{k=1}^{3} \frac{\partial}{\partial x_k}\frac{\partial X_k}{\partial s_j} = \sum_{k=1}^{3} \mathbb{F}_{kj}\frac{\partial}{\partial x_k} \tag{B.21}$$

Plugging this identity into (B.20) and letting $\delta\widetilde{X}_i(\mathbf{x},t) = \delta X_i(\mathbf{X}^{-1}(\mathbf{x},t))$ we get

$$\int_{\Omega_0}\left(\frac{\delta E}{\delta \mathbf{X}} - \frac{\delta \widehat{E}}{\delta \mathbf{X}}\right)\cdot \delta\mathbf{X} d\mathbf{s} = \sum_{i,j,k=1}^{3}\int_{\Omega}\left[\frac{\partial W}{\partial J}\mathbb{F}_{kj}\mathbb{F}_{ji}^{-1}\right]\Big|_{\mathbf{s}=\mathbf{X}^{-1}(\mathbf{x},t)}\frac{\partial \delta\widetilde{X}_i}{\partial x_k}d\mathbf{x} \tag{B.22}$$

$$= \sum_{i=1}^{3}\int_{\Omega}\frac{\partial W}{\partial J}\Big|_{\mathbf{s}=\mathbf{X}^{-1}(\mathbf{x},t)}\frac{\delta\widetilde{X}_i}{\partial x_i}d\mathbf{x} \tag{B.23}$$

We used $\sum_{j=1}^{3}\mathbb{F}_{ji}\mathbb{F}_{kj}^{-1} = \delta_{ik}$ in the last equality.

Let $q(\mathbf{x},t) = -\frac{\partial W}{\partial J}\Big|_{\mathbf{s}=\mathbf{X}^{-1}(\mathbf{x},t)}$. Using integration by parts and assuming that the boundary terms vanish we get

$$\int_{\Omega_0}\left(\frac{\delta E}{\delta \mathbf{X}} - \frac{\delta \widehat{E}}{\delta \mathbf{X}}\right)\cdot \delta\mathbf{X} d\mathbf{s} = \int_{\Omega}\nabla_{\mathbf{x}} q(\mathbf{x},t)\cdot\delta\widetilde{\mathbf{X}}d\mathbf{x} \tag{B.24}$$

Using the change of variables $\mathbf{x} = \mathbf{X}(\mathbf{s},t)$ on the integral on the left and using the definition of $\mathbf{f}(\mathbf{x},t)$ and $\hat{\mathbf{f}}(\mathbf{x},t)$ gives

$$\int_{\Omega}(\mathbf{f}(\mathbf{x},t) - \hat{\mathbf{f}}(\mathbf{x},t))\cdot\delta\widetilde{\mathbf{X}}(\mathbf{x},t)d\mathbf{x} = \int_{\Omega}\nabla_{\mathbf{x}}q(\mathbf{x},t)\cdot\delta\widetilde{\mathbf{X}}(\mathbf{x},t)d\mathbf{x} \tag{B.25}$$

Since $\delta\widetilde{\mathbf{X}}(\mathbf{x},t)$ is arbitrary,

$$\mathbf{f}(\mathbf{x},t) - \hat{\mathbf{f}}(\mathbf{x},t) = \nabla_{\mathbf{x}}q(\mathbf{x},t) \tag{B.26}$$

Appendix C

These notes can be found in [5]; they are reproduced here for convenience.

On a given element T, let $\mathbf{s}^{(k_0)}$, $\mathbf{s}^{(k_1)}$, $\mathbf{s}^{(k_2)}$, $\mathbf{s}^{(k_3)}$ denote the vertices of T in the reference configuration and let $\mathbf{X}^{(k_0)}$, $\mathbf{X}^{(k_1)}$, $\mathbf{X}^{(k_2)}$, $\mathbf{X}^{(k_3)}$ denote the vertices of T in the deformed configuration.

We have

$$\widetilde{X}_i - X_i^{(k_0)} = \sum_{j=1}^{3} a_{ij}(s_j - s_j^{(k_0)}) \tag{C.1}$$

where the a_{ij} are determined by

$$X_i^{(k_1)} - X_i^{(k_0)} = \sum_{j=1}^{3} a_{ij}(s_j^{(k_1)} - s_j^{(k_0)}) \tag{C.2}$$

$$X_i^{(k_2)} - X_i^{(k_0)} = \sum_{j=1}^{3} a_{ij}(s_j^{(k_2)} - s_j^{(k_0)}) \tag{C.3}$$

$$X_i^{(k_3)} - X_i^{(k_0)} = \sum_{j=1}^{3} a_{ij}(s_j^{(k_3)} - s_j^{(k_0)}) \tag{C.4}$$

For each $i = 1, 2,$ or 3, we have 3 equations in the 3 unknowns a_{i1}, a_{i2}, a_{i3}. Let $\mathbf{a}_i$ be the vector with these unknowns as its components. The three equations may then be written

$$X_i^{(k_1)} - X_i^{(k_0)} = \mathbf{a}_i\cdot(\mathbf{s}^{(k_1)} - \mathbf{s}^{(k_0)}) \tag{C.5}$$

$$X_i^{(k_2)} - X_i^{(k_0)} = \mathbf{a}_i\cdot(\mathbf{s}^{(k_2)} - \mathbf{s}^{(k_0)}) \tag{C.6}$$

$$X_i^{(k_3)} - X_i^{(k_0)} = \mathbf{a}_i\cdot(\mathbf{s}^{(k_3)} - \mathbf{s}^{(k_0)}) \tag{C.7}$$

Look for a solution of the form

$$\mathbf{a}_i = \lambda_1(\mathbf{s}^{(k_2)} - \mathbf{s}^{(k_0)})\times(\mathbf{s}^{(k_3)} - \mathbf{s}^{(k_0)}) + \lambda_2(\mathbf{s}^{(k_3)} - \mathbf{s}^{(k_0)})\times(\mathbf{s}^{(k_1)} - \mathbf{s}^{(k_0)}) + \lambda_3(\mathbf{s}^{(k_1)} - \mathbf{s}^{(k_0)})\times(\mathbf{s}^{(k_2)} - \mathbf{s}^{(k_0)})$$

Then

$$X_i^{(k_1)} - X_i^{(k_0)} = \lambda_1 V_z \tag{C.8}$$

$$X_i^{(k_2)} - X_i^{(k_0)} = \lambda_2 V_z \tag{C.9}$$

$$X_i^{(k_3)} - X_i^{(k_0)} = \lambda_3 V_z \tag{C.10}$$

where

$$V_z = (\mathbf{s}^{(k_2)} - \mathbf{s}^{(k_0)}) \times (\mathbf{s}^{(k_3)} - \mathbf{s}^{(k_0)}) \cdot (\mathbf{s}^{(k_1)} - \mathbf{s}^{(k_0)}) \tag{C.11}$$

is the signed volume of the tetrahedron T in its reference configuration. (The scalar V_z may be negative since we do not assume any particular order in enumerating the vertices of T.)

Then

$$\mathbf{a}_i = \frac{1}{6V_z}[(X_i^{(k_1)} - X_i^{(k_0)})(\mathbf{s}^{(k_2)} - \mathbf{s}^{(k_0)}) \times (\mathbf{s}^{(k_3)} - \mathbf{s}^{(k_0)}) + (X_i^{(k_2)} - X_i^{(k_0)})(\mathbf{s}^{(k_3)} - \mathbf{s}^{(k_0)}) \times (\mathbf{s}^{(k_1)} - \mathbf{s}^{(k_0)}) + (X_i^{(k_3)} - X_i^{(k_0)})(\mathbf{s}^{(k_1)} - \mathbf{s}^{(k_0)}) \times (\mathbf{s}^{(k_2)} - \mathbf{s}^{(k_0)})]$$

The derivatives $\partial a_{ij}/\partial \mathbf{X}^{(k_l)}$ can be calculated from this expression. Note that only the ith component of the vector $\partial a_{ij}/\partial \mathbf{X}^{(k_l)}$ is nonzero. Thus,

$$\frac{\partial a_{ij}}{X_i^{(k_0)}} = \frac{-1}{6V_z}[(\mathbf{s}^{(k_2)} - \mathbf{s}^{(k_0)}) \times (\mathbf{s}^{(k_3)} - \mathbf{s}^{(k_0)}) + (\mathbf{s}^{(k_3)} - \mathbf{s}^{(k_0)}) \times (\mathbf{s}^{(k_1)} - \mathbf{s}^{(k_0)}) + (\mathbf{s}^{(k_1)} - \mathbf{s}^{(k_0)}) \times (\mathbf{s}^{(k_2)} - \mathbf{s}^{(k_0)})]$$

$$\frac{\partial a_{ij}}{X_i^{(k_1)}} = \frac{1}{6V_z}(\mathbf{s}^{(k_2)} - \mathbf{s}^{(k_0)}) \times (\mathbf{s}^{(k_3)} - \mathbf{s}^{(k_0)})$$

$$\frac{\partial a_{ij}}{X_i^{(k_2)}} = \frac{1}{6V_z}(\mathbf{s}^{(k_3)} - \mathbf{s}^{(k_0)}) \times (\mathbf{s}^{(k_1)} - \mathbf{s}^{(k_0)})$$

and

$$\frac{\partial a_{ij}}{X_i^{(k_3)}} = \frac{1}{6V_z}(\mathbf{s}^{(k_1)} - \mathbf{s}^{(k_0)}) \times (\mathbf{s}^{(k_2)} - \mathbf{s}^{(k_0)})$$

Appendix D. Discretization of an elastic shell

We begin with a coarse triangulation of the unit sphere generated by taking a regular icosahedron whose vertices are on the unit sphere. To refine this triangulation, we take the midpoints of the edges, project them onto the unit sphere, and connect these projected midpoints to the vertices of the triangles to divide each triangle into four triangles. This refinement process may be repeated as many times as needed to obtain a sufficiently fine triangulation of the sphere. This triangulation (scaled as needed) will be used repeatedly in the construction that follows.

The thick elastic shell is divided into several layers. Each layer is discretized using the same tetrahedral mesh structure, and the tetrahedral mesh for the elastic shell is the union of the meshes for the layers. The triangulation for the unit sphere is the starting point for the construction of the tetrahedral mesh. To construct a mesh for a given layer, generate a triangulation for the inner and outer sphere of the layer simply by scaling the triangulation of the unit sphere. Next, take the centroids of the triangles from either one of the two triangulations and project them onto a sphere halfway between the inner and outer sphere. The vertices of the two triangulations and the centroids form the vertices of the tetrahedral mesh in a single layer. See Fig. D.17A.

Having defined all of the nodes of a layer, we need only say which pairs of nodes are connected by edges to define our tetrahedral mesh, since a tetrahedron is then defined by any set of four vertices of which any two are connected by an edge. Of course, the edge assignments are not arbitrary, since one must check that no two tetrahedra overlap, and also that there are no gaps between the tetrahedra within the layer. The following edge assignments satisfy these criteria.

Within the inner sphere and the outer sphere of a layer, we use the edge connections of the original triangulation (Fig. D.17A). Within the central sphere of the layer, each node is the image of a centroid of one of the original triangles, and we connect each such centroid to the centroids of its neighboring triangles (Fig. D.17C). We also connect each centroid to all of the nodes on the inner and outer sphere that are images of the vertices of its own triangle (Fig. D.17B). Finally, we make a radial connection between every node on the inner sphere to its image node on the outer sphere (Fig. D.17D).

In our construction, all of the layers had the same thickness h_l, which was chosen to obtain the best aspect ratio for the tetrahedral mesh as a whole. For each tetrahedron, the ratio of the maximum edge length to the insphere radius was used for the aspect ratio; this number was normalized so a regular tetrahedron had an aspect ratio of 1. The aspect ratio of the entire tetrahedral mesh was taken to be the maximum of the aspect ratios of the tetrahedra in the mesh [12]. We let $h_l = \beta_{3D} h_t$,

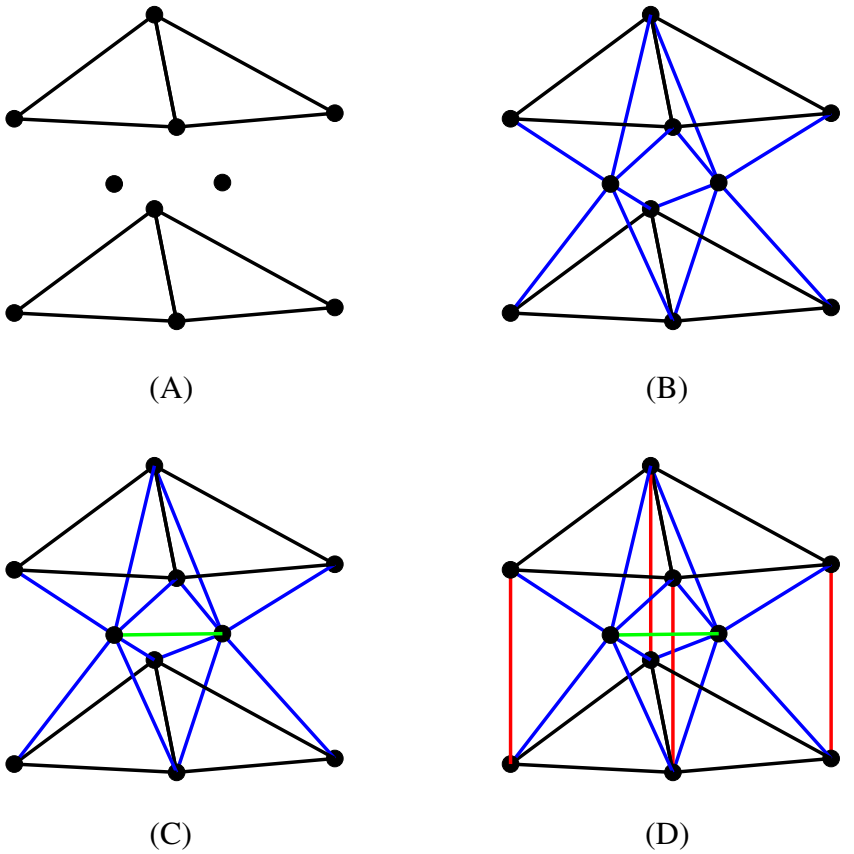

Fig. D.17. Schematic for the edge connections within the tetrahedral mesh. (A) A portion of the triangulation for the outer sphere, its corresponding triangulation for the inner sphere, and the centroids corresponding to the triangles projected onto the central sphere are shown. The vertices of the two triangulations and the centroids are the nodes in the tetrahedral mesh. The edges in the triangulations form one set of edge connections in the tetrahedral mesh. (B) Centroids are connected to the vertices of their corresponding triangles (denoted by blue lines). (C) Centroids are connected to centroids of neighboring triangles (denoted by green lines). (D) Each vertex on the triangulation for the outer sphere is connected to its image in the triangulation for the inner sphere (denoted by red lines). (For interpretation of the references to color in this figure legend, the reader is referred to the web version of this article.)

where h_t is the length of the longest edge in the outer sphere triangulation, and chose β_{3D} so that the aspect ratio of the tetrahedral mesh is close to 1. We used $\beta_{3D} = 1.2$.

For the tetrahedral mesh of the thick elastic shell used in the simulations, the triangulation of the outer sphere was generated by refining the coarse triangulation described above 4 times and scaling the resulting triangulation. The tetrahedral mesh contained 16 layers (corresponding to $h_l = 1.2h_t$) so that each fluid grid cell intersecting the elastic shell contains approximately 8 vertices from the tetrahedral mesh. (Recall that each 'layer' actually has two layers of tetrahedra.)

References

[1] D.M. McQueen, C.S. Peskin, Heart simulation by an immersed boundary method with formal second-order accuracy and reduced numerical viscosity, in: Proceedings of the ICTAM, 2000.
[2] T. Belytschko, W.K. Liu, B. Moran, Nonlinear Finite Elements for Continua and Structures, first ed., John Wiley and Sons, Ltd., New York, 2000.
[3] C.S. Peskin, The immersed boundary method, Acta Numer. 11 (2002) 479–517.
[4] B.E. Griffith, On the volume conservation of the immersed boundary method, Commun. Comput. Phys. 12 (2012) 401–432.
[5] C.S. Peskin, The immersed boundary method. III. Energy functions for the representation of immersed elastic boundaries and materials, handwritten lecture notes available from http://math.nyu.edu/faculty/peskin/iblecturenotes/index.html, 2007.
[6] I. Doghri, Mechanics of Deformable Solids: Linear, Nonlinear, Analytical, and Computational Aspects, first ed., Springer-Verlag, Berlin, 2000.
[7] J. Merodio, R.W. Ogden, Mechanical response of fiber-reinforced incompressible non-linearly elastic solids, Int. J. Nonlinear Mech. 40 (2005) 213–227.
[8] M.E. Rosar, C.S. Peskin, Fluid flow in collapsible elastic tubes: a three-dimensional numerical model, New York J. Math. 7 (2001) 281–302.
[9] M-C Lai, C.S. Peskin, An immersed boundary method with formal second order accuracy and reduced numerical viscosity, J. Comput. Phys. 160 (2000) 705–719.
[10] D.M. McQueen, C.S. Peskin, Heart simulation by an immersed boundary method with formal second-order accuracy and reduced numerical viscosity, in: H. Aref, J.W. Phillips (Eds.), Mechanics for a New Millennium, Proceedings of the International Conference on Theoretical and Applied Mechanics (ICTAM)2000, Kluwer Academic Publishers, 2001.

[11] D. Boffi, L. Gastaldi, L. Heltai, C.S. Peskin, On the hyper-elastic formulation of the immersed boundary method, Comput. Methods Appl. Mech. Engrg. 197 (2008) 2210–2231.
[12] V.N. Parthasarathy, C.M. Graichen, A.F. Hathaway, A comparison of tetrahedron quality measures, Finite Elem. Anal. Design 15 (1993) 255–261.
[13] Y. Kim, C.S. Peskin, Numerical study of incompressible fluid dynamics with nonuniform density by the immersed boundary method, Phys. Fluids 20 (2008).
[14] L. Zhu, C.S. Peskin, Simulation of a flapping flexible filament in a flowing soap film by the immersed boundary method, J. Comput. Phys. 179 (2002) 452–468.
[15] Y. Mori, C.S. Peskin, Implicit second order immersed boundary methods with boundary mass, Comput. Methods Appl. Mech. Engrg. 197 (2008) 2049–2067.
[16] X. Wang, W.K. Liu, Extended immersed boundary method using FEM and RKPM, Comput. Methods Appl. Mech. Engrg. 193 (2004) 1305–1321.